Hydrogen diffusion in $TiCr_2H_x$ Laves phases: A combined ab initio and machine-learning-potential study

Pranav Kumar 👓a,*, Fritz Körmann 👓b,c, Kaveh Edalati 👓d,e,f, Blazej Grabowski 👓a, Yuji Ikeda 👓a,*

^aInstitute for Materials Science, University of Stuttgart, Pfaffenwaldring 55, 70569, Stuttgart, Germany ^bInterdisciplinary Centre for Advanced Materials Simulation (ICAMS), Ruhr-Universität Bochum, 44801, Bochum, Germany ^cDepartment of Computational Materials Design, Max-Planck-Institut for Sustainable Materials, 40237, Düsseldorf, Germany ^d WPI, International Institute for Carbon-Neutral Energy Research (WPI-I2CNER), Kyushu University, 819-0395, Fukuoka, Japan

b Interdisciplinary Centre, for Advanced Materials Simulation (ICAMS), Ruba-University, 4591, Internal, 45911, Internal properties of Computational Materials Design, MacPlanck, Institut for Sustainable Materials, 45915, Stakoba, Japan 4WII, International Institute for Carbon-Neutral Research (WPL-ISCNER), Kyusha University, 819-6395, Pukuoka, Japan 1Mitsni Chemicals, Inc. - Carbon-Neutral Research Center (MCI-CNRC), Kyusha University, 819-6395, Fukuoka, Japan 1Mitsni Chemicals, Inc. - Carbon-Neutral Research Center (MCI-CNRC), Kyusha University, 819-6395, Fukuoka, Japan 1Mitsni Chemicals, Inc. - Carbon-Neutral Research Center (MCI-CNRC), Kyusha University, 819-6395, Fukuoka, Japan 1Mitsni Chemicals, Inc. - Carbon-Neutral Research Center (MCI-CNRC), Kyusha University, 819-6395, Fukuoka, Japan 1Mitsni Chemicals, Inc. - Carbon-Neutral Research Center (MCI-CNRC), Kyusha University, 819-6395, Fukuoka, Japan 1Mitsni Chemicals, Inc. - Carbon-Neutral Research Center (MCI-CNRC), Kyusha University, 819-6395, Fukuoka, Japan 1Mitsni Chemicals, Inc. - Carbon-Neutral Research Center (MCI-CNRC), Kyusha University, 819-6395, Fukuoka, Japan 1Mitsni Chemicals, Inc. - Carbon-Neutral Research Center (MCI-CNRC), Kyusha University, 819-6395, Fukuoka, Japan 1Mitsni Chemicals, Inc. - Carbon-Neutral Research Center (MCI-CNRC), Kyusha University, 819-6395, Fukuoka, Japan 1Mitsni Chemicals, Inc. - Carbon-Neutral Research Center (MCI-CNRC), Kyusha University, 819-6395, Fukuoka, Japan 1Mitsni Chemicals, Inc. - Carbon-Neutral Research Center (MCI-CNRC), Kyusha University, 819-6395, Fukuoka, Japan 1Mitsni Chemicals, Inc. - Carbon-Neutral Research Center (MCI-CNRC), Kyusha University, 819-6395, Fukuoka, Japan 1Mitsni Chemicals, Inc. - Carbon-Neutral Research Center (MCI-CNRC), Kyusha University, 819-6395, Fukuoka, Japan 1Mitsni Chemicals, Inc. - Carbon-Neutral Research Center (MCI-CNRC), Kyusha University, 819-6395, Fukuoka, Japan 1Mitsni Chemicals, Inc. - Carbon-Neutral Research Center (MCI-CNRC), Kyusha University, 819-6395, Fukuoka, Japan

The diffusion of hydrogen plays a critical role in determining the kinetic performance of hydrogen-storage materials and has therefore been the subject of extensive investigations. Specifically for TiCr₂ in its Laves phases, proton at 313-442 K, comparable to the value obtained from the NMR study for the same C15 phase with a similar hydrogen concentration [17]. Mazzolai et al. [19] investigated hydrogen diffusion in $TiCr_{1.78}H_x$ for a dilute hydrogen concentration ($x \approx 0.017$) using internal friction and hydrogen absorption measurements. They reported that the activation barrier can reach up to 0.60 eV at 660–1200 K, i.e., a value substantially larger than those obtained by the other

^{*}Corresponding authors

Email addresses: pranav.kumar@imw.uni-stuttgart.de (Pranav Kumar), yuji.ikeda@imw.uni-stuttgart.de (Yuji

experiments [17, 18, 20]. It is challenging to interpret the scatter in the activation barriers from experiments alone.

Atomistic simulations based on density functional theory (DFT) can provide further insight into the hydrogen diffusion properties. Indeed, several computational studies have quantified the energetics and migration barriers of hydrogen in the $TiCr_2$ Laves phases [16, 21–23]. However, most existing computational works have focused on dilute solution energies and provided only a limited analysis of migration barriers between A₂B₂ sites. Moreover, quantitative assessments of hydrogen diffusion coefficients in TiCr₂ Laves phases across a wide range of hydrogen concentrations are largely absent from prior computational studies. This is primarily due to the high computational cost of DFT. Accurately resolving hydrogen distribution and interactions requires large length and time scales, which makes ab initio molecular dynamics (MD) simulations computationally prohibitive.

Recent advancements in machine learning interatomic potentials (MLIPs) now allow MD simulations at larger spatial and temporal scales while retaining near-DFT accuracy. MD simulations employing MLIPs have indeed been successfully applied to the investigation of atomic diffusion, such as hydrogen [24–29] and lithium [30, 31]. In our previous study [32], we developed MLIPs for studying hydrogenated TiCr₂ Laves phases. The developed MLIPs accurately account for a wide range of hydrogen concentrations while capturing the precise energetics involved.

In the present study, we systematically investigate hydrogen migration and diffusion in C15 and C14 TiCr₂ using DFT and MLIPs. With DFT, we quantify hydrogen migration barriers for all possible symmetrically inequivalent paths between face-sharing interstitial sites. MD simulations are performed to investigate diffusion coefficients of hydrogen using MLIPs trained on DFT data. In particular, we analyze how the hydrogen diffusion coefficients depend on hydrogen concentration and temperature in both the C15 and the C14 phases.

2. Methodology

2.1. Crystal structures and interstitial sites

The Ti–Cr system reveals the C15 and the C14 Laves phases near the TiCr₂ composition in experiments [35–38]. The low-temperature C15 phase has a cubic symmetry belonging to the space group 227 $(Fd\bar{3}m)$. The high-temperature C14 phase has a hexagonal symmetry belonging to the space group 194 $(P6_3/mmc)$. Table 1 summarizes the ideal positions of the metal atoms as well as the interstitial sites in the C15 and the C14 Laves phases. In such AB₂ Laves phases, hydrogen atoms may be accommodated in three chemically distinct tetrahedral interstitial site types, i.e., B₄, AB₃, and A₂B₂, characterized by four surrounding metal atoms. The numbers of symmetrically in-equivalent interstitial site sublattices in the C15 cubic and C14 hexagonal Laves phases are three and seven, respectively.

Table 1: Fractional coordinates of the metal atoms (A and B) and the interstitial sites (B₄, AB₃, and A₂B₂) in the AB₂ Laves phases. The C15 cubic and the C14 hexagonal Laves phases show symmetries of the space groups $Fd\bar{3}m$ (227) and $P6_3/mmc$ (194), respectively. The positions in the C15 phase are given with the origin choice 2, i.e., the origin set at the inversion center. The subscripts at the Wyckoff letters distinguish the interstitial sites and follow the notation of Shoemaker and Shoemaker [33]. The values in bold are constrained by symmetry, while the others refer to the ideal case of a close-packed hard-sphere model with an atomic-radius ratio of $r_A/r_B = (3/2)^{1/2} \approx 1.225$ [34] and a c/a ratio of $(8/3)^{1/2} \approx 1.633$ for the C14 phase. The positions of the interstitial sites are given as the geometric centers of the surrounding four metal atoms.

	Type	Wyckoff	x	y	z
C15	A B	8a $16d$	$\begin{array}{c} 1/8 \\ 1/2 \end{array}$	$\begin{array}{c} 1/8 \\ 1/2 \end{array}$	$\begin{array}{c} 1/8 \\ 1/2 \end{array}$
	$_{ m B_4}$	8b	3/8	3/8	3/8
	AB_3	32e	9/32	9/32	9/32
	A_2B_2	96g	5/16	5/16	1/8
C14	A B	4f $2a$ $6h$	$1/3 \\ 0 \\ -1/6$	${f 2/3} \\ {f 0} \\ -2/6$	$1/16 \\ 0 \\ 1/4$
	B_4	4e	0	0	3/16
	AB_3	$4f$ $12k_1$	1/3 1/8	2/3 1/4	43/64 23/64
	A_2B_2	$6h_1 \\ 6h_2 \\ 12k_2 \\ 24l$	5/24 11/24 13/24 1/24	5/12 11/12 13/12 1/3	1/4 1/4 1/8 9/16

2.2. Hydrogen migration barriers from DFT

DFT calculations conducted were using VASP 6.2.1 [39–41] with a plane-wave basis and with the projector augmented-wave (PAW) method [42]. The exchange-correlation energy was obtained using the generalized gradient approximation (GGA) in the Perdew-Burke-Ernzerhof (PBE) form [43]. The valence electron configurations in the PAW potentials were $[\text{Ne}]3s^23p^64s^23d^2$, $[\text{Ar}]4s^13d^5$ and $1s^1$ for Ti, Cr, and H atoms, respectively. The plane-wave energy cutoff was set to 400 eV. Unless otherwise specified, all calculations were conducted with supercell models of a $2 \times 2 \times 2$ expansion of the primitive C15 unit cell and a $2 \times 2 \times 1$ expansion of the C14 unit cell, each containing 48 metal atoms, as visualized in Figure 1. The reciprocal space was sampled with a Γ -centered k-point mesh of $4 \times 4 \times 4$ for both the C15 and the C14 supercell models along with the Methfessel-Paxton smearing [44] with a width of 0.1 eV. Electronic self-consistent-field iterations were performed until the energy convergence threshold of 1×10^{-5} eV was reached. Spin-polarization was not considered, as it does not affect the energies and the forces on atoms at any hydrogen concentration relevant to the present study [32].

In the dilute hydrogen limit (single hydrogen in the simulation cell), there are a total of 4 and 11 symmetrically distinct migration paths between first-nearest-neighbor face-sharing tetrahedral interstitial sites for the C15 cubic and C14 hexagonal phases, respectively, as detailed in Sec. 3.2. The minimum-energy paths for these migra-

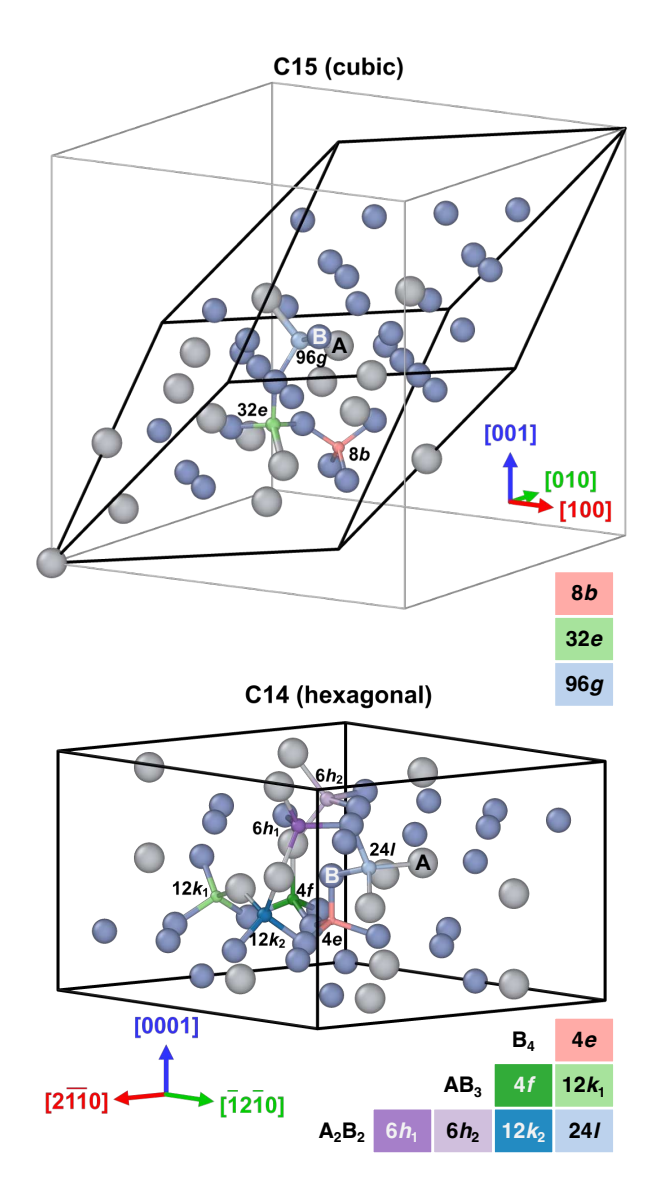


Figure 1: 48-metal-atom cells of the C15 cubic and the C14 hexagonal Laves phases together with symmetrically distinct interstitial sites. Ti–H bonds are depicted thicker than Cr–H bonds to indicate that the former requires higher energies to break during hydrogen migration (cf. Sec. 3.2). The gray-colored cell for C15 represents a cubic supercell surrounding the 48-metal-atom cell.

tion paths were calculated using the generalized solid-state nudged elastic band (G-SSNEB) method [45], as implemented in the VTST software [46, 47]. For the initial and final configurations of each minimum-energy path, a single hydrogen atom was placed at the corresponding interstitial site in the 48-metal-atom supercell, and then all atomic positions and cell vectors were optimized to their ground state, resulting in volumetric distortion relative to pristine TiCr₂. Between the initial and final states, 11 linearly interpolated intermediate images were generated and connected by a spring constant of 5 eV/Å². The atomic positions and cell shapes of the intermediate images were further optimized using the quick-min method [48] with a time step of 0.1 fs and a force convergence criterion of $1\times 10^{-2}\,\mathrm{eV/Å}$.

2.3. Fine-tuning of MLIPs for diffusion

In the present study, we started with two previously developed MLIPs for the TiCr₂ Laves phases with hydrogen [32], corresponding to the C14 phase (C14-MTP) and the C15 phase (C15-MTP). These MLIPs, specifically moment tensor potentials (MTPs) [49], reproduce the DFT energies with an accuracy of approximately $3\,\mathrm{meV/atom}$ for a wide range of hydrogen concentrations, i.e., TiCr₂H_x where 0 < x < 6.

The original C14-MTP, however, required refinement in order to achieve stable and accurate diffusion calculations at high hydrogen concentrations of $x \geq 3.5$. Specifically, C14-MTP occasionally generated unrealistically large forces, which caused hydrogen atoms to undergo unphysical displacements. To address this issue, we implemented the following iterative fine-tuning protocol based on active learning. First, classical MD simulations were performed in the canonical (NVT) ensemble at 1000 K using the original C14-MTP. During these simulations, the extrapolation grade [50–52] was continuously monitored as a measure of the potential's reliability. During each MD simulation, configurations with extrapolation grades above 2.1 were continuously extracted and saved. The simulation was terminated once the extrapolation grade exceeded 10. The saved configurations were re-filtered to identify additional configurations required to construct the active set [50–52] based on D-optimality. The energies, forces, and stresses of these additional configurations were computed with single-point DFT calculations, and the thus labeled configurations were incorporated into the original training dataset. The MTP was then retrained on this augmented dataset. This active-learning process was repeated with the updated MTP until no additional configurations exhibited extrapolation grades above the selection threshold of 2.1 during 0.1 ns of the MD simulations for all the investigated hydrogen concentrations. Through this finetuning, 101 new configurations were added to the training dataset, increasing its size from $18\,902$ to $19\,003$ structures. At the end, the fine-tuned C14-MTP successfully resolved the stability issues of the original potential, enabling robust and reliable MD simulations of hydrogen diffusion at high hydrogen concentrations.

In contrast, the previously developed C15-MTP [32] for modeling the C15 phase exhibited stable MD simulations up to x=4 in ${\rm TiCr_2H}_x$, and therefore no fine-tuning was required.

2.4. Diffusion coefficients of hydrogen from MD

The hydrogen diffusion coefficient was computed from the mean squared displacement (MSD) of hydrogen atoms in an MD simulation. The MSD was evaluated as

$$MSD(t) = \frac{1}{N_{H}} \sum_{i=1}^{N_{H}} |\mathbf{r}_{i}(t) - \mathbf{r}_{i}(0)|^{2}, \qquad (1)$$

where $\mathbf{r}_i(t)$ denotes the position of atom i at time t, and $N_{\rm H}$ is the number of hydrogen atoms. The MSD can be

assumed to depend on t as

$$MSD(t) \propto t^{\alpha}$$
. (2)

When the MD simulation time is sufficiently long, the system enters the normal-diffusion regime, and α becomes approximately equal to 1, i.e., the MSD depends linearly on t. The diffusion coefficient D is then obtained from the long-time limit of the MSD according to the Einstein equation [53] as

$$D = \lim_{t \to \infty} \frac{\text{MSD}(t)}{6t}.$$
 (3)

The MD simulations were conducted in simulation cells with 6000 metal atoms obtained by a $5 \times 5 \times 5$ expansion of the original 48-metal-atom supercell models, with the size of the simulation cells determined based on a convergence test for the diffusion coefficient (Appendix A). In the MD simulations, hydrogen atoms were initially distributed among the interstitial sites randomly. Each system was subsequently equilibrated using the isothermalisobaric (NPT) ensemble with a time step of 1 fs and a duration of 50–1500 ps depending on temperature. The simulations were then switched to the microcanonical (NVE)ensemble for over 1 ns up to 5 ns. Temperatures of 250 K, 400 K, 500 K, 700 K and 1000 K and eight hydrogen concentrations in $0 < x \le 4$ for $TiCr_2H_x$ were considered. To ensure converged statistics, the MD simulations were conducted twice for 250 K and five times for the other temperatures. The α values in Eq. (2) were first examined to see whether the MD simulation time reached the normal-diffusion regime. As detailed in Sec. 3.3, the MD simulations reached the normal-diffusion regime at all the temperatures except for 250 K, and therefore the diffusion coefficients were obtained at temperatures of 400 K and above following Eq. (3).

The MD simulations were carried out using LAMMPS [54] with the MTPs. In most simulations, the MLIP-2 interface [55] was used. For simulations at 400 K, another recently developed implementation [56] was employed, yielding approximately a twofold speedup over the MLIP-2 interface on CPUs.

The C14 Laves phase has hexagonal symmetry, and therefore its hydrogen diffusion coefficients are expected to be anisotropic. As detailed in Appendix B, however, the anisotropy in C14 $\mathrm{TiCr_2H_x}$ is found to be negligible at temperatures of 400 K and above, and therefore averaged isotropic diffusion coefficients are discussed in the main text.

In general, quantum effects substantially affect hydrogen diffusion in various systems. In most cases, quantum tunneling reduces the activation barriers at low temperatures, which causes a temperature-induced transition of the dominant diffusion scheme, resulting in a non-Arrhenius trend [57–60]. Specifically for ${\rm TiCr_2}$ in the Laves phases, Miwa and Asahi [22] investigated hydrogen diffusion in C15 ${\rm TiCr_2H_{1.3}}$ at room temperature using the

Table 2: Binding energies $E_{\rm b}$ of a single hydrogen atom at the interstices of the C15 cubic and the C14 hexagonal TiCr₂ Laves phases obtained with DFT [32].

	Type	Site	$E_{ m b}~({ m meV/H})$
C15	B_4	8b	+599
	AB_3	32e	-16
	A_2B_2	96g	-217
C14	B_4	4e	+566
	AB_3	$\begin{array}{c} 4f \\ 12k_1 \end{array}$	$^{+77}_{-19}$
	A_2B_2	$6h_1 \\ 6h_2 \\ 12k_2 \\ 24l$	$-170 \\ -249 \\ -173 \\ -185$

path integral hybrid Monte Carlo method [61–63] in combination with an MLIP trained with DFT data and elucidated the lowering of the activation barriers compared with classical MD results. On the other hand, Mazzolai et al. [19] reported that, in experiments, quantum effects on hydrogen diffusion in C14 $\mathrm{TiCr}_{1.78}\mathrm{H}_x$ at a dilute hydrogen concentration ($x\approx0.017$) are prominent around 120 K while moderate around room temperature. As our primary focus in the present work is on how the diffusion coefficients depend on hydrogen concentration, we performed classical MD simulations mainly at temperatures above room temperature, where quantum effects play only a minor role.

3. Results and Discussion

3.1. Interstitial site preferences in the TiCr₂ Laves phases

Table 2 summarizes the binding energies of single isolated hydrogen atoms in the C15 cubic and the C14 hexagonal Laves phases reproduced from our previous DFT study [32]. In both the C15 and the C14 phases, hydrogen solubility is highest at the A_2B_2 -type interstitial sites, followed by the AB_3 - and B_4 -type sites in decreasing order. This preference is consistent with previous computational and experimental studies, which report that hydrogen predominantly occupies the A_2B_2 sites in $TiCr_2$ [21, 64] and other Laves-phase alloys [2, 16, 65, 66]. In the C14 hexagonal phase, the tetrahedral interstices are further classified into seven symmetrically distinct ones. Among the four A_2B_2 sites in C14, the $6h_2$ site is the most favorable for hydrogen, followed by the other three sites.

3.2. Hydrogen migration barriers

The C15 cubic and the C14 hexagonal Laves phases exhibit 4 and 11 symmetrically distinct first-nearest-neighbor (1NN) face-sharing interstitial pairs, respectively, between which hydrogen atoms may migrate. Table 3 shows the migration energies of a single hydrogen atom for all the symmetrically distinct migration paths in the TiCr₂ Laves phases obtained from DFT in conjunction with the G-SSNEB method. The minimum-energy paths for these

Table 3: Hydrogen migration energies $E_{\rm mig}$ of all symmetrically distinct paths in the TiCr₂ Laves phases obtained using DFT.

	S_1	S_2		Bond b	reaking	E_{mig} (meV)	
		_		$S_1 \to S_2$	$S_2 \to S_1$	$S_1 \to S_2$	$S_2 \to S_1$
C15	8b (B ₄) 32e (AB ₃) 96g (A ₂ B ₂) 96g (A ₂ B ₂)	32e (AB ₃) 96g (A ₂ B ₂) 96g (A ₂ B ₂) 96g (A ₂ B ₂)	B_3 AB_2 AB_2 A_2B	B–H B–H A–H B–H	A–H A–H A–H B–H	190 90 286 119	805 291 286 119
C14	4e (B ₄) 4e (B ₄) 4f (AB ₃) 4f (AB ₃) 12k ₁ (AB ₃) 12k ₁ (AB ₃) 6h ₁ (A ₂ B ₂) 6h ₂ (A ₂ B ₂) 12k ₂ (A ₂ B ₂) 24l (A ₂ B ₂) 24l (A ₂ B ₂)	$\begin{array}{cccc} 90g & (A_2B_2) \\ \hline & 4e & (B_4) \\ 12k_1 & (AB_3) \\ 4f & (AB_3) \\ 12k_2 & (A_2B_2) \\ 6h_1 & (A_2B_2) \\ 24l & (A_2B_2) \\ 12k_2 & (A_2B_2) \\ 24l & (A_2B_2) \end{array}$	B ₃ B ₃ B ₃ AB ₂ AB ₂ AB ₂ A ₂ A ₂ B A ₂ A ₂ B A ₂ A ₂ B A ₂ B A ₂ B	B-H B-H A-H B-H B-H B-H A-H B-H A-H B-H	B-H A-H A-H A-H A-H B-H A-H B-H A-H B-H	119 154 154 635 111 98 97 86 280 111 314 99	119 154 739 635 362 249 264 165 203 123 314 99

migration paths and the comparison with the migration barriers obtained with current MLIPs are presented in the SM. Additionally, Fig. 2 visually summarizes these migration paths, together with the migration energies.

The migration energy for each path is qualitatively characterized by the bond that needs to be broken during the migration; a Ti-H bond requires a higher energy to break than a Cr-H bond. Specifically, the migration energies involving the breaking of a Ti-H bond span $286-805\,\mathrm{meV}$ and $203-739\,\mathrm{meV}$ for the C15 and the C14 phases, respectively. In contrast, the migration energies involving the breaking of a Cr-H bond span 90-190 meV and 86–165 meV for the C15 and the C14 phases, respectively. This demonstrates higher chemical affinity of Ti for H than that of Cr for H. Since A and B in other typical AB₂ Laves-phase alloys also tend to show higher and lower chemical affinity with H, respectively, the trend derived above may also hold for these Laves-phase alloys, i.e., the migrations involving the breaking of an A-H bond also likely show higher migration barriers than the migrations involving the breaking of a B-H bond.

A distinction between the migrations involving the breaking of Ti–H and Cr–H bonds is particularly important for the C15 96g–96g and the C14 24l–24l paths. For each of these pairs, there are two symmetrically distinct paths: one with the breaking of a Ti–H bond and the other with the breaking of a Cr–H bond. The migration energies of the paths with the Ti–H breaking are $286 \,\mathrm{meV}$ and $314 \,\mathrm{meV}$ for the C15 96g–96g and the C14 24l–24l pairs, respectively, while the migration energies of the paths with the Cr–H breaking are $119 \,\mathrm{meV}$ and $99 \,\mathrm{meV}$ for the C15 96g–96g and the C14 24l–24l pairs, respectively. This exemplifies the importance of considering not only the symmetry of each end point but also the symmetry of the path in between when evaluating the hydrogen migration between the interstitial sites.

The migrations from the AB₃ to the B₄ sites require much higher migration energies than the others; the migration energy from the 32e to the 8b sites in the C15 phase is 805 meV, and the migration energy from the 4f to the 4e sites in the C14 phase is $739\,\mathrm{meV}$. It is therefore unlikely that hydrogen atoms visit the B_4 sites during diffusion.

The paths among the A₂B₂ and the AB₃ interstitial sites in each Laves phase make a network, as visualized in Fig. 3. The network consists of cages, each of which surrounds an A atom and is topologically analogous to the C₂₈ fullerene [67]. The cages in each Laves phase further build a super-network in a similar manner as the A atoms, i.e., cubic and hexagonal diamond networks for the C15 and the C14 Laves phases, respectively. Each cage contains four hexagonal rings consisting of A₂B₂ sites sharing A₂B faces. A hydrogen jump among these sites involves the breaking of a B–H bond. In contrast, a hydrogen jump escaping from a hexagonal ring involves the breaking of an A–H bond, which requires a higher energy than a B–H bond. Therefore, the migration barriers of the inter-ring jumps are higher than those of the intra-ring jumps.

In the C14 hexagonal Laves phase, due to the symmetrical distinction among the A₂B₂ interstitial sites (cf. Sec. 2.1), each cage has two distinct types of hexagonal rings. Specifically, among the four hexagonal rings in each cage, one consists of $6h_1$ and $6h_2$ sites and the other three consist of $12k_2$ and 24l sites. In the case of C14 TiCr₂ investigated in the present study, among the inter-ring jumps, the $6h_2$ -to- $6h_1$ migration shows the highest migration barrier (165 meV), followed by 24l-to- $12k_2$ (123 meV), $12k_2$ -to-24l (111 meV), 24l-to-24l (99 meV), and $6h_1$ -to- $6h_2$ (86 meV) jumps in descending order (cf. Sec. 3.2). This indicates that, within the hexagonal rings, hydrogen atoms at the $6h_2$ sites may take the longest time to jump, as also expected from the most negative binding energies at the $6h_2$ site (cf. Sec. 3.1). In consequence, the characteristics of hydrogen diffusion are more sophisticated in the C14 hexagonal TiCr₂ than in the C15 cubic counterpart (cf. Appendix B). The detailed impact of the symmetrically distinct sites in the C14 Laves phase can vary with its chemical composition, and hence we may find different trends for other Laves-phase alloys.

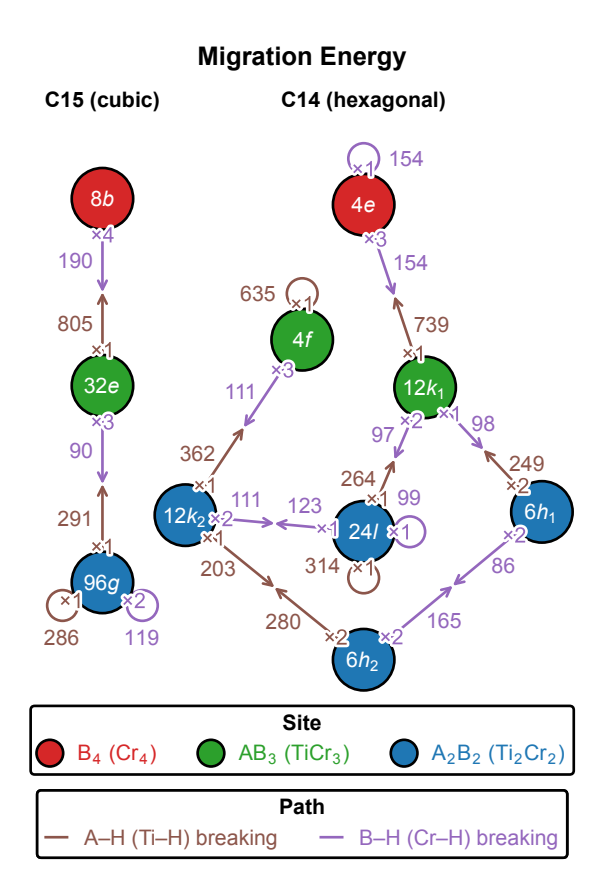


Figure 2: All symmetrically distinct migration paths between face-sharing interstitial sites in the dilute limit (single hydrogen atom in the simulation cell). Arrows correspond to the available paths for hydrogen to migrate between two sites, along with their multiplicities and hydrogen migration barriers (meV) in Table 3. Loops indicate migration between the sites of the same type.

3.3. Mean squared displacements of hydrogen

To investigate hydrogen diffusion at finite hydrogen concentrations, we performed MD simulations using the C15-MTP and the fine-tuned C14-MTP (cf. Sec. 2.3).

We first examined if the hydrogen diffusion reaches the normal-diffusion regime via Eq. (2). Figure 4 illustrates the evolution of the MSD in $\mathrm{TiCr_2H_{1.0}}$ over MD time at five different temperatures: $250\,\mathrm{K}$, $400\,\mathrm{K}$, $500\,\mathrm{K}$, $750\,\mathrm{K}$ and $1000\,\mathrm{K}$. At and above $400\,\mathrm{K}$, as time progresses, the slope of the MSD with respect to MD time in the log–log scale, i.e., α in Eq. (2), converges to 1, indicating that the MD simulations reach the normal-diffusion regime where the diffusion coefficients can be evaluated via Eq. (3). In contrast, the MSDs at $250\,\mathrm{K}$ exhibit reduced slopes and fail to reach the normal-diffusion regime within the nanosecond time scale accessible in MD simulations. The same trend is found for the other hydrogen concentrations (cf. Sec. S2 in the SM).

Figure 5 shows the trajectories of hydrogen atoms in ${\rm TiCr_2H_{1.0}}$ at both 250 K and 500 K after an MD simulation time of 0.1 ns. At 250 K, almost all hydrogen atoms remain confined within the hexagonal rings made of ${\rm A_2B_2}$ sites due to the respective lower migration barriers, rarely

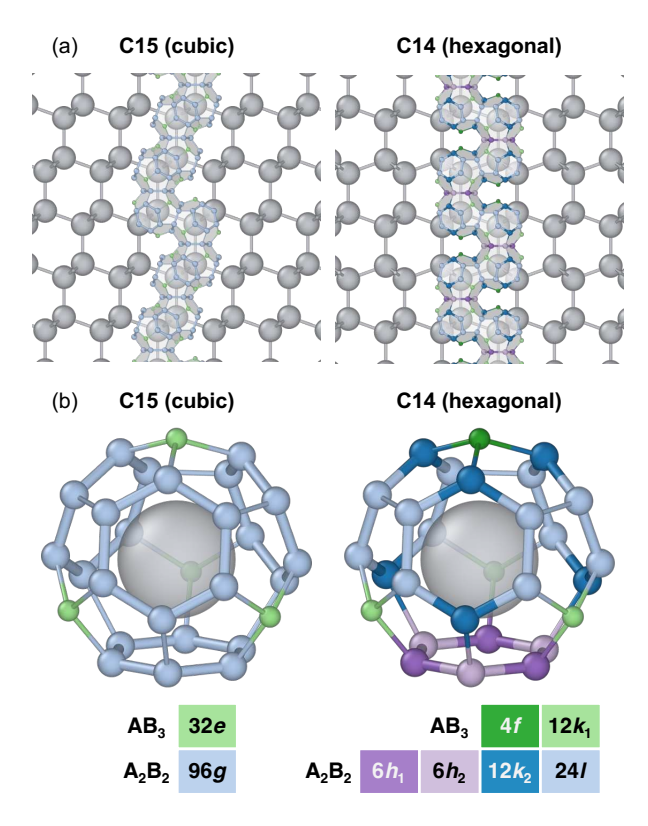


Figure 3: Cages of A_2B_2 and AB_3 interstitial sites surrounding A atoms in the AB_2 Laves phases, which correspond to the diffusion pathways of hydrogen. Colored spheres represent interstitial sites, where the A_2B_2 sites are shown as larger spheres compared to the AB_3 sites. Bonds between the interstitial-site spheres represent possible migration paths for hydrogen atoms, where thicker bonds show low-migration-energy paths within hexagonal rings associated with B-H bond breaking, and thinner bonds denote high-migration-energy paths requiring A-H bond breaking when jumping from the A_2B_2 sites. In the C15 Laves phase, the 96g sites form low-migration-energy hexagonal rings. In the C14 Laves phase, the $6h_1-6h_2$ and the $12k_2-24l$ sites form symmetrically distinct low-migration-energy hexagonal rings. (a) Part of the super-network of the cages in each Laves phase. (b) Expansion of a single cage in each Laves phase.

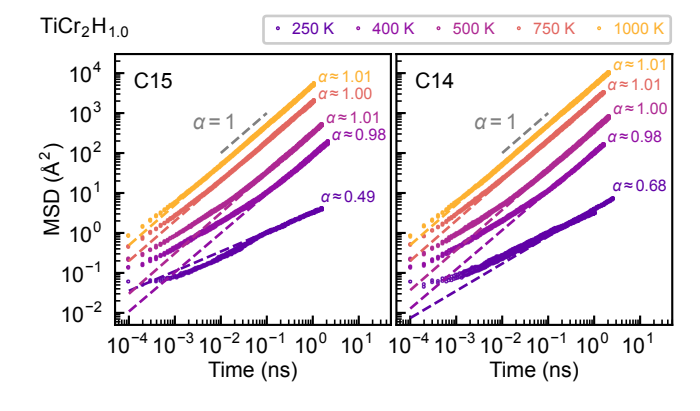


Figure 4: MSDs of hydrogen atoms in ${\rm TiCr_2H_{1.0}}$ as a function of MD simulation time.

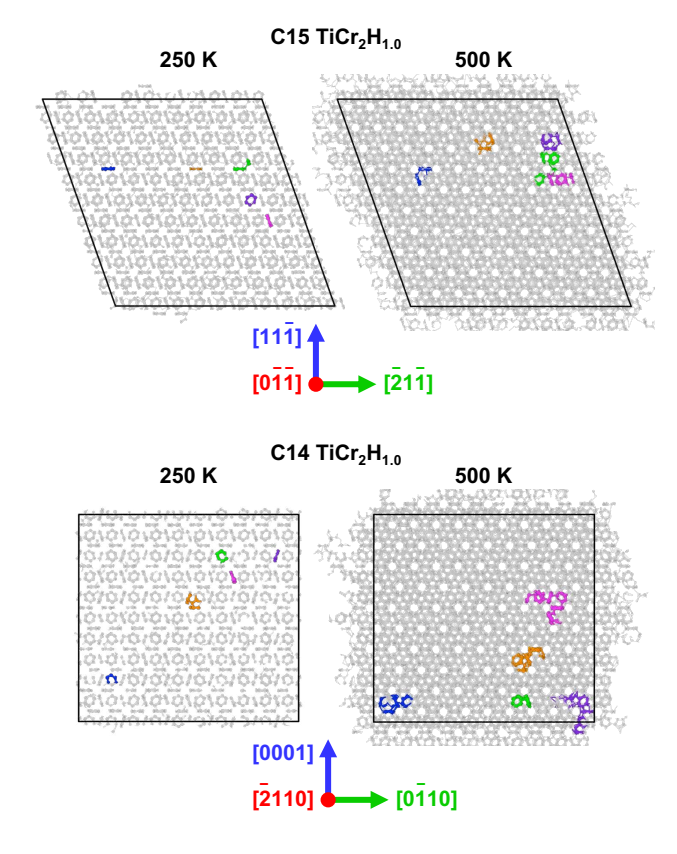


Figure 5: Trajectories of hydrogen atoms in C15 and C14 $\rm TiCr_2H_{1.0}$ during MD simulations. Gray lines represent the trajectories of all hydrogen atoms over 0.1 ns of simulation, while thick colored lines highlight the individual trajectories of five randomly selected hydrogen atoms.

migrating to neighboring hexagonal rings. Inter-ring migrations are necessary for hydrogen to reach the normal-diffusion regime, but their occurrence is statistically insufficient at this low temperature even after 1 ns of MD simulation time (Fig. 4). In contrast, at 500 K, most hydrogen atoms undergo multiple inter-ring migrations, thereby clearly exhibiting long-range diffusion. This confirms that the system is in the normal-diffusion regime for hydrogen.

3.4. Dependence on hydrogen concentration

We next discuss the dependence of hydrogen diffusion coefficients on hydrogen concentration. As detailed in Sec. 3.3, at 250 K, the systems did not reach the normal-diffusion regime within the MD simulation time, and therefore we could not obtain the diffusion coefficients via Eq. (3). Note also that quantum effects could be substantial at such low temperatures (cf. Sec. 2.4). We have therefore computed diffusion coefficients only at higher temperatures. Figure 6 presents the diffusion coefficients D of hydrogen at four temperatures as a function of x in $\mathrm{TiCr_2H_x}$. (The raw values of D are provided in the SM.)

For each temperature and each hydrogen concentration, the diffusion coefficients tend to be lower in the C15 cubic phase than the C14 hexagonal phase, but only slightly. This reflects the geometrical similarity of the

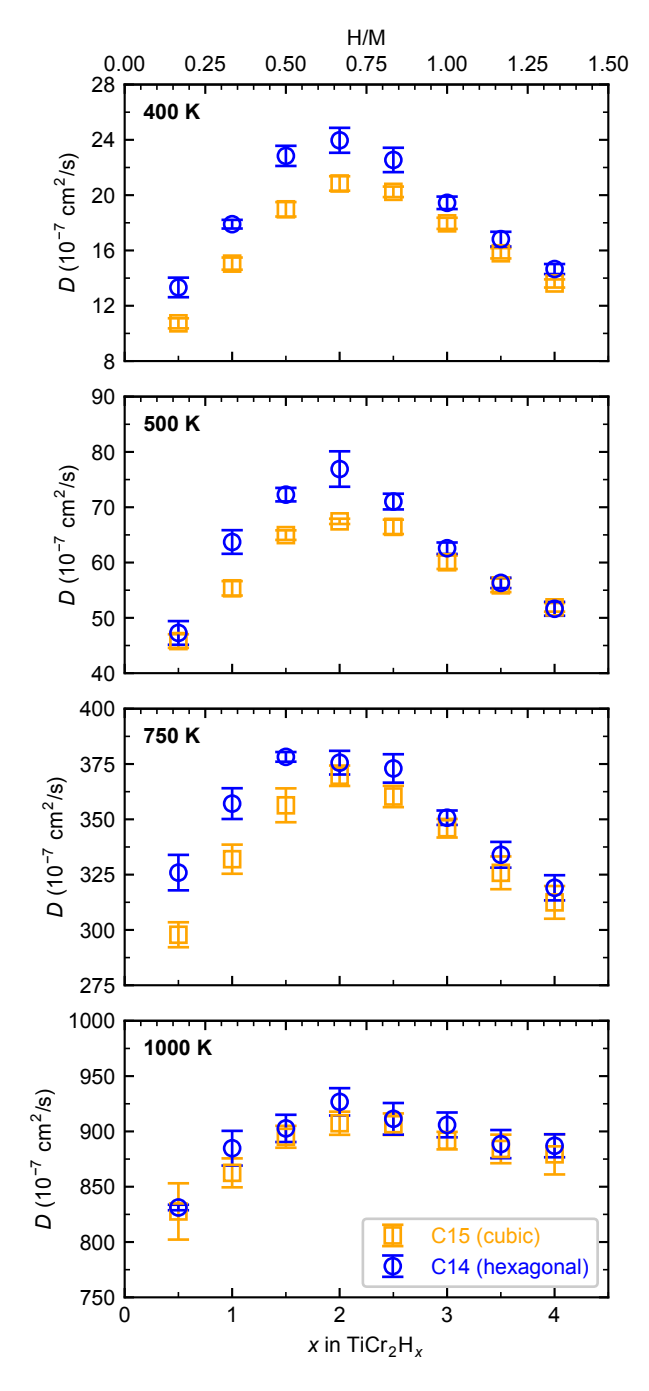


Figure 6: Diffusion coefficients of hydrogen atoms as a function of hydrogen concentration in TiCr₂ at four temperatures. Error bars represent the standard deviations obtained from five independent MD simulations.

two Laves phases, where topologically only the stacking sequences are different [68].

For all temperatures, the diffusion coefficient D substantially depends on the hydrogen concentration x. This dependence is non-monotonic; D increases for $0 < x \le 2$ and decreases for $2 \le x \le 4$ with increasing x. The dependence on hydrogen concentration is more evident at lower temperatures. At the highest considered temperature of $1000\,\mathrm{K}$, the diffusion coefficient increases modestly

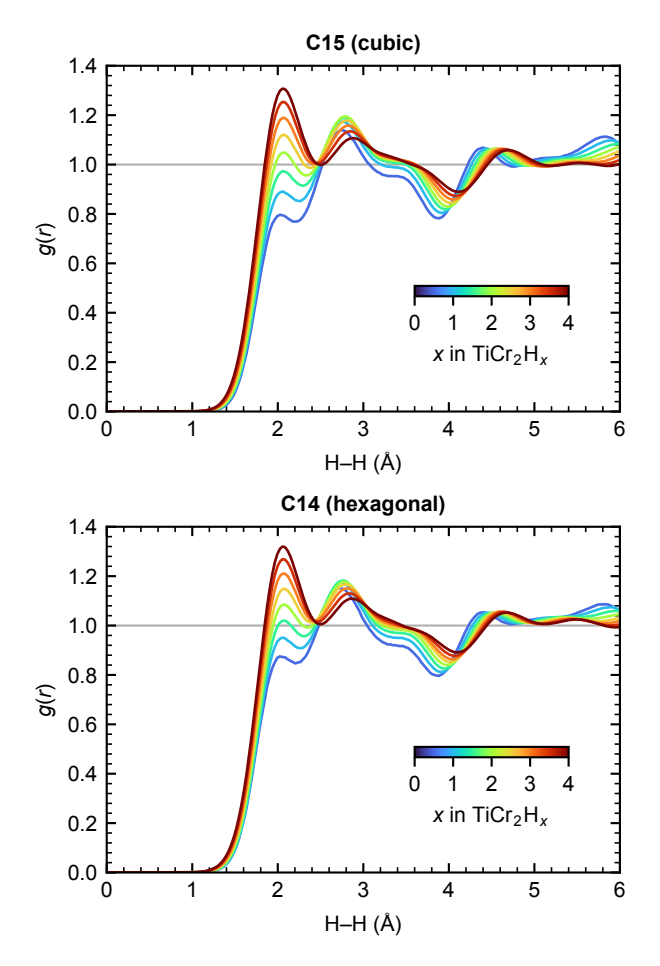


Figure 7: Time averaged RDFs for the H–H pairs in ${\rm TiCr_2H_x}$ obtained with the MD simulations at $1000\,{\rm K}$.

by 13% in the C15 phase and 10% in the C14 phase when x increases from 0.5 to 2.0. At 400 K, the increases are much larger, accounting for 94% and 80% in the C15 and the C14 phases, respectively, within the same x range.

To investigate the trend of hydrogen occupation at the interstitial sites and its impact on diffusion coefficients, we also calculated the time-averaged radial distribution functions (RDFs) of hydrogen atoms to analyze their occupancy trends at 1000 K, as visualized in Figure 7. The time-averaging was conducted over the last 50 ps of one of the five MD trajectories used for the diffusion-coefficient calculations.

For each hydrogen concentration, the time-averaged RDFs reveal two prominent peaks: one near 2.1 Å, corresponding to the Switendick limit for H–H separation, and another around 2.7–2.8 Å. There are no peaks around 1.6 Å, i.e., the distances between the 1NN face-sharing interstitial sites [33]. This indicates that the face-sharing positions are rarely occupied during hydrogen diffusion, likely due to strong repulsion between hydrogen atoms at these positions [32]. Therefore, the first peak near 2.1 Å primarily arises from hydrogen atoms in the second-nearest-neighbor (2NN) edge-sharing interstitial sites, while the second peak reflects occupancy at more distant sites.

At a low hydrogen concentration of x = 0.5, hydrogen atoms tend to occupy isolated positions, as evidenced by the lower height of the first peak in the RDFs compared to the second peak. As the hydrogen concentration increases, the height of the first peak grows progressively, while the second peak remains nearly saturated. This enhancement of the first peak indicates that hydrogen atoms increasingly occupy the 2NN edge-sharing interstitial sites, resulting in stronger repulsion between hydrogen atoms. This repulsive interaction influences hydrogen diffusion in two regimes. For x < 2, the growing collective repulsion acts as an internal driving force that lowers the effective activation barrier for hydrogen migration between interstitial sites, thereby enhancing diffusion. Around $x \approx 2$, the first RDF peak reaches a height comparable to the height of the second peak, indicating that the local hydrogen concentrations at the edge-sharing positions become nearly equal to the average hydrogen concentrations in the systems. The diffusion coefficients become highest around this concentration, as found in Fig. 6. For x > 2, the continued increase of the first peak reflects excessive crowding, where intense repulsion between hydrogen atoms restricts hydrogen migration. That is, an unoccupied interstitial site with more than one adjacent site occupied by hydrogen atoms is blocked so that one of these hydrogen atoms cannot migrate into the unoccupied site due to the strong repulsion with the other hydrogen atoms at the face-sharing positions. This eventually leads to the declines in diffusion coefficients.

3.5. Comparison with experiments

Figure 8 shows the computed hydrogen diffusion coefficients of $TiCr_2H_x$ as a function of inverse temperature across different hydrogen concentrations. The MD simulations reveal that, across the entire investigated temperature range above 400 K, the diffusion coefficients at each hydrogen concentration show an Arrhenius-type dependence. As discussed in Sec. 3.4, at a fixed temperature, the diffusion coefficients show a non-monotonic dependence on hydrogen concentration. Thus, the diffusion coefficients in Fig. 8 are distributed in the shaded region, and the corresponding activation barriers lie in the range 0.21–0.25 eV. These activation barriers are in good agreement with many experimental values. Specifically, Hiebl [20] obtained 0.2–0.3 eV with proton and deuteron NMR measurements for C15 $TiCr_{1.85}H_{0.8}$ above 250 K. Campbell *et al.* [18] obtained 0.24 eV with quasi-elastic neutron scattering for C15 $TiCr_{1.85}H_{0.43}$ at 313-442 K. Bowman et al. [17] obtained 0.13–0.26 eV and 0.205–0.40 eV for C15 $\mathrm{TiCr}_{1.8}\mathrm{H}_x$ (x = 0.55, 2.58) and C14 TiCr_{1.9}H_x (x = 0.63, 2.85), respectively, above 180 K. In contrast, Mazzolai et al. [19] reported an activation energy of approximately 0.6 eV for C14 TiCr_{1.78}H_{0.017} at temperatures at 660–1200 K, determined from pressure—time measurements for hydrogen absorption. This high value was interpreted as evidence of classical over-barrier hopping, in contrast to the low- and intermediate-temperature hydrogen dynamics probed by

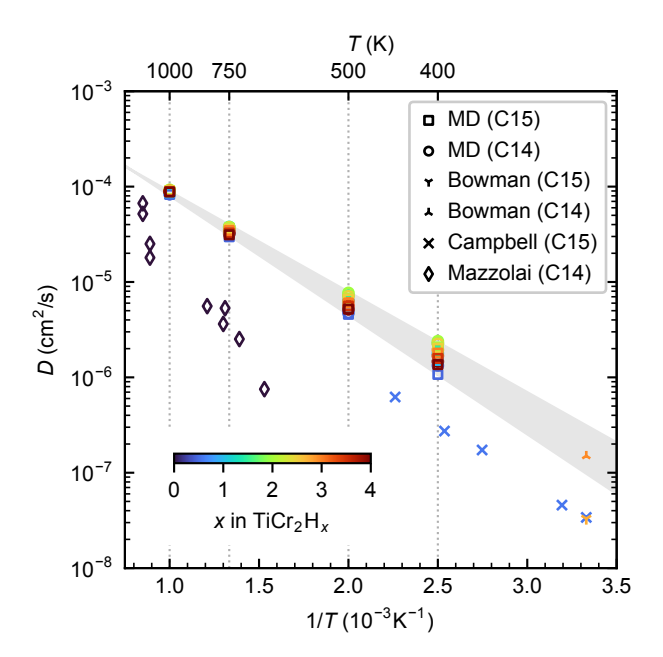


Figure 8: Diffusion coefficients of hydrogen atoms in $\mathrm{TiCr_2H_x}$ in the C15 and the C14 Laves phases as a function of inverse temperature, calculated through MD simulations. The colors of the points represent the hydrogen concentration x as specified by the color scale. The shaded region indicates the range of diffusion coefficients for varying hydrogen concentrations. Experimental values for C15 $\mathrm{TiCr_{1.8}H_{2.58}}$ and C14 $\mathrm{TiCr_{1.9}H_{2.85}}$ reported by Bowman et al. [17], C15 $\mathrm{TiCr_{1.85}H_{0.43}}$ reported by Campbell et al. [18], and C14 $\mathrm{TiCr_{1.85}H_{0.017}}$ reported by Mazzolai et al. [19] are also included for comparison.

NMR, QENS, or internal friction. However, our present MD results actually show an Arrhenius-type trend over a wide temperature range of 400–1000 K. We would therefore ascribe the exceptionally high activation barrier in Ref. [19] rather to difficulties of the respective experimental approach in determining the intrinsic hydrogen diffusion coefficients. In further support, we note that other binary Laves phases also show activation barriers in the range 0.13–0.26 eV in experiments [69], consistently with the present MD simulations.

Despite the agreement of the computed activation barrier with the experimental values, the MD simulations show diffusion coefficients one order of magnitude higher than the experimental values, particularly those of Campbell et al. [18]. The most likely reason for the discrepancy is the non-stoichiometric compositions of metal atoms in experiments, i.e., $TiCr_{1.8}$ for the C15 phase [12] and $TiCr_{1.9}$ for the C14 phase [13], which are not considered in the present MD simulations. The non-stoichiometric compositions require either Cr vacancies or Ti anti-sites at the Cr sites. Indeed, vacancies in metallic systems can act as hydrogen traps [70]. Also, anti-site Ti indicates a higher ratio of the A₂B₂ (Ti₂Cr₂) interstitial sites than those in the stoichiometric composition, which show larger binding energies than the other types of interstitial sites (cf. Sec. 3.1) and thus possibly slow down hydrogen kinetics. Intrinsic errors in the exchange-correlation

functional in DFT can be another reason [71]. Specifically, the PBE functional tends to underestimate the binding energies among atoms [72], which may result in overestimation of diffusion coefficients. Note also that the experimental values of Bowman et al. [17] show diffusion coefficients that differ by one order of magnitude for C15 TiCr_{1.8}H_{2.58} (3.4 × 10⁻⁸ cm²/s) and C14 TiCr_{1.9}H_{2.85} (1.5 × 10⁻⁷ cm²/s) at 300 K. While the former agrees well with the values of Campbell et al., the latter is within the range expected from the present MD simulations based on the Arrhenius relationship extrapolated to 300 K.

4. Conclusions

In this work, we have elucidated the mechanisms of hydrogen diffusion in $\mathrm{TiCr}_2\mathrm{H}_x$ Laves phases $(0 < x \le 4)$ and revealed that complex H–H interactions lead to changes in diffusion coefficients with hydrogen concentration.

The DFT-calculated migration barriers in the dilute hydrogen limit exhibit substantially different hydrogen migration energies even among the A_2B_2 sites. Specifically, the activation barriers for the paths involving the breaking of a Ti-H bond are substantially higher than those involving the breaking of a Cr-H bond, demonstrating higher chemical affinity of Ti for H than that of Cr.

The MD simulations across varying hydrogen concentrations reveal a non-monotonic dependence of diffusion coefficients on hydrogen content, which is more pronounced at lower temperatures. Time-averaged RDFs of hydrogen atoms indicate that hydrogen atoms avoid occupying 1NN face-sharing positions even during diffusion. As the hydrogen concentration increases, more 2NN edgesharing interstitial sites get occupied, leading to an increase in H–H repulsion. This repulsive interaction influences hydrogen diffusion in two regimes. At lower hydrogen concentrations (x < 2), the repulsion interaction acts as a driving force to reduce the activation barrier. At higher hydrogen concentrations (x > 2), the repulsion blocks the remaining interstitial sites from being occupied, hindering hydrogen migration.

The MD-derived diffusion coefficients exhibit an Arrhenius-type behavior in the investigated temperature range (400–1000 K), with activation barriers in good agreement with most experimental values. In contrast, the diffusion coefficients are approximately one order of magnitude higher than most experimental values. The discrepancy is likely due to hydrogen trapping by defects such as Cr vacancies and Ti anti-sites in the non-stoichiometric $TiCr_2$ compositions in experiments, not captured in the present MD simulations.

The above findings provide various atomistic insights into hydrogen diffusion in TiCr₂. The gained knowledge may also be transferable to multi-component Laves phases for more practical hydrogen storage applications, providing guidance to tailor hydrogen kinetics for fast hydrogen absorption and desorption.

CRediT authorship contributions

Pranav Kumar: Conceptualization, Methodology, Software, Validation, Formal Analysis, Investigation, Data Curation, Writing – Original Draft, Visualization. Fritz Körmann: Writing – Review & Editing. Kaveh Edalati: Writing – Review & Editing. Blazej Grabowski: Resources, Funding Acquisition, Writing – Review & Editing. Yuji Ikeda: Conceptualization, Software, Visualization, Writing – Review & Editing, Supervision, Project Administration, Funding Acquisition.

Declaration of Generative AI and AI-assisted technologies in the writing process

ChatGPT and Grammarly were used to assist with initial drafting and sentence refinement for certain sections of this manuscript. The authors subsequently reviewed and edited all content as needed and take full responsibility for the final version of the publication.

Declaration of competing interest

The authors declare that they have no known competing financial interests or personal relationships that could have appeared to influence the work reported in this paper.

Acknowledgments

Pranav Kumar and Yuji Ikeda are funded by the Deutsche Forschungsgemeinschaft (DFG, German Research Foundation), Project No. 519607530. Fritz Körmann acknowledges support by the Heisenberg Programme of the Deutsche Forschungsgemeinschaft (DFG, German Research Foundation), Project No. 541649719. Blazej Grabowski acknowledges funding from the European Research Council (ERC) under the European Union's Horizon 2020 research and innovation programme (grant agreement No. 865855). The authors also acknowledge support by the state of Baden–Württemberg through bwHPC and the DFG through grant no INST 40/575-1 FUGG (JUSTUS 2 cluster) and the SFB1333 (project ID 358283783-CRC 1333/2 2022).

Appendix A. Impact of supercell size on diffusion coefficients

In this appendix, we investigate the effect of supercell size on the diffusion coefficients of hydrogen, taking C15 $\mathrm{TiCr_2H_{3.0}}$ as an example. Specifically, we examined further $n \times n \times n$ (n=1, 2, 3, 4, 5) expansions of the original 48-metal-atom cells (cf. Sec. 2.1). MD simulations were performed at 1000 K. The system was initially equilibrated for 50 ps in the NPT ensemble, followed by the calculation of the MSD for 1 ns in the NVE ensemble. Figure A.1 shows the thus obtained diffusion coefficients of

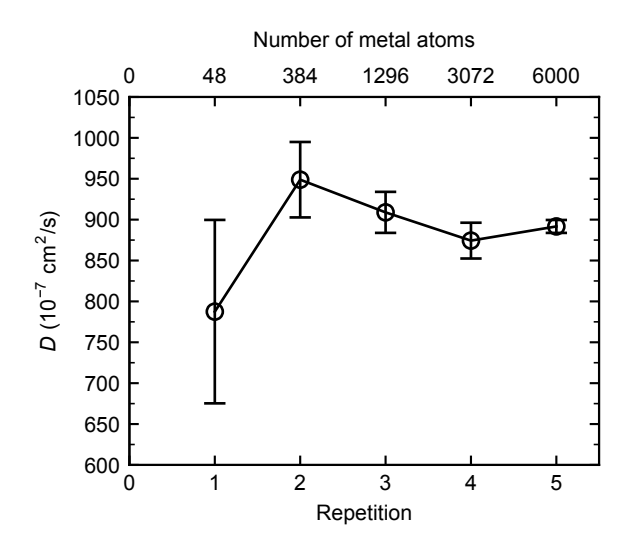


Figure A.1: Diffusion coefficient of C15 $\rm TiCr_2H_{3.0}$ as a function of supercell size. Error bars represent the standard deviations obtained from five independent MD simulations.

hydrogen in C15 TiCr₂H_{3.0} as a function of supercell size. As the supercell size increases, the number of hydrogen atoms also increases, providing better statistical sampling and leading to diffusion coefficients with reduced uncertainty. With 6000 metal atoms, i.e., for the $5\times5\times5$ repetition of the original 48-metal-atom cells, the uncertainty of the diffusion coefficient is less than 1%. We therefore use the 6000-metal-atom cells for the investigation of diffusion coefficients in the present study.

Appendix B. Anisotropy of hydrogen diffusion in C14 TiCr₂

Since the C14 Laves phase has hexagonal symmetry, in principle the hydrogen diffusion coefficients are isotropic and should show differences between the directions perpendicular and parallel to the [0001] direction. In this appendix, we investigate the degree of anisotropy of hydrogen diffusion via the hydrogen MSDs resolved into the contribution of a direction perpendicular to [0001]

$$MSD_{\perp}(t) = \frac{1}{N_{H}} \sum_{i=1}^{N_{H}} \frac{1}{2} \left(|x_{i}(t) - x_{i}(0)|^{2} + |y_{i}(t) - y_{i}(0)|^{2} \right)$$
(B.1)

and that along [0001]

$$MSD_{\parallel}(t) = \frac{1}{N_{\rm H}} \sum_{i=1}^{N_{\rm H}} |z_i(t) - z_i(0)|^2,$$
 (B.2)

where the z axis is set along the [0001] direction. Five MD simulations, independent of those for the main-text results, were run for ${\rm TiCr_2H_{1.0}}$ at temperatures of 250 K, 400 K, 500 K, 750 K and 1000 K under the same MD conditions as those in the main text. Figure B.2 presents the ${\rm MSD_{\parallel}/MSD_{\perp}}$ ratios obtained from the MD simulations.

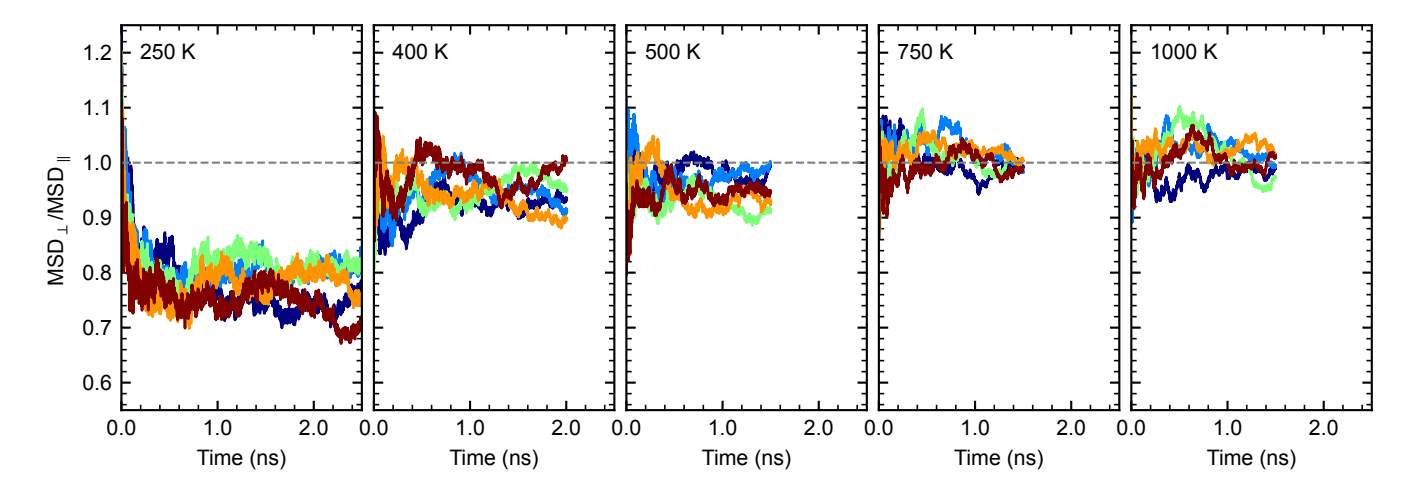


Figure B.2: Ratio of MSDs of hydrogen atoms parallel and perpendicular to the [0001] direction in C14 TiCr₂H_{1.0} from five independent MD simulations at different temperatures.

At 250 K, where hydrogen does not reach the normal-diffusion regime within an MD simulation time of 2.5 ns (cf. Sec. 3.3), MSD_{\parallel} is substantially smaller than MSD_{\perp} , with the $MSD_{\parallel}/MSD_{\perp}$ ratios in a range of 0.7–0.8. This indicates that, in the given short time scale, hydrogen tends to be more trapped along the [0001] direction compared with the directions perpendicular to [0001] (cf. Sec. 3.3). This happens maybe because more hydrogen are trapped in the $6h_1$ – $6h_2$ rings than the $12k_2$ -24l rings (cf. Sec. 3.2). That is, the $6h_2$ sites show substantially more negative hydrogen binding energies than the other A_2B_2 sites (cf. Sec. 3.1) and show the highest migration barriers than the other paths within the hexagonal rings (cf. Sec. 3.2). Since the $6h_1$ – $6h_2$ rings lie perpendicular to the [0001] direction, they does not contribute to MSD_{\parallel} .

At temperatures of 400 K and above—where the $\stackrel{\parallel}{\text{MD}}$ simulations reach the normal-diffusion regime—the ratio of MSD_{\parallel} to MSD_{\perp} converges to values between 0.9 and 1.1. This suggests that, in contrast to the short length scale, long-range hydrogen diffusion in C14 TiCr₂ is essentially isotropic at the higher temperatures.

Data availability

The developed MTPs along with the corresponding DFT training datasets are freely accessible on DaRUS.

References

- [1] F. Stein, A. Leineweber, Laves phases: a review of their functional and structural applications and an improved fundamental understanding of stability and properties, Journal of Materials Science 56 (9) (2021) 5321–5427. doi:10.1007/s10853-020-05509-2.
- URL https://doi.org/10.1007/s10853-020-05509-2
 [2] V. A. Yartys, M. V. Lototskyy, Laves type intermetallic compounds as hydrogen storage materials: A review, Journal of Alloys and Compounds 916 (2022) 165219. doi:10.1016/j.jallcom.2022.165219.
 - URL https://www.sciencedirect.com/science/article/pii/ S0925838822016103

- [3] P. Edalati, R. Floriano, A. Mohammadi, Y. Li, G. Zepon, H.-W. Li, K. Edalati, Reversible room temperature hydrogen storage in high-entropy alloy TiZrCrMnFeNi, Scripta Materialia 178 (2020) 387-390. doi:10.1016/j.scriptamat.2019.12.009. URL https://www.sciencedirect.com/science/article/pii/S1359646219307286
- [4] A. Mohammadi, Y. Ikeda, P. Edalati, M. Mito, B. Grabowski, H.-W. Li, K. Edalati, High-entropy hydrides for fast and reversible hydrogen storage at room temperature: Binding-energy engineering via first-principles calculations and experiments, Acta Materialia 236 (2022) 118117. doi:10.1016/j.actamat. 2022.118117.
 - URL https://www.sciencedirect.com/science/article/pii/ S1359645422004980
- [5] N. Ding, W. Liu, B. Chen, S. Wang, S. Zhao, Q. Wang, C. Wang, D. Yin, L. Wang, Y. Cheng, Interface and body engineering via aluminum hydride enabling Ti-V-Cr-Mn alloy with enhanced hydrogen storage performance, Chemical Engineering Journal 470 (2023) 144143. doi:10.1016/j.cej.2023.144143. URL https://www.sciencedirect.com/science/article/pii/S1385894723028747
- [6] R. B. Strozi, B. H. Silva, D. R. Leiva, C. Zlotea, W. J. Botta, G. Zepon, Tuning the hydrogen storage properties of Ti-V-Nb-Cr alloys by controlling the Cr/(TiVNb) ratio, Journal of Alloys and Compounds 932 (2023) 167609. doi:10.1016/j.jallcom. 2022.167609. URL https://www.sciencedirect.com/science/article/pii/

S0925838822040002

S1385894724040932

- [7] S. Dangwal, Y. Ikeda, B. Grabowski, K. Edalati, Machine learning to explore high-entropy alloys with desired enthalpy for room-temperature hydrogen storage: Prediction of density functional theory and experimental data, Chemical Engineering Journal 493 (2024) 152606. doi:10.1016/j.cej.2024.152606. URL https://www.sciencedirect.com/science/article/pii/
- [8] G. Andrade, P. Edalati, S. Dangwal, K. Edalati, R. Floriano, Microstructural Characterization and Hydrogen Storage Properties at Room Temperature of Ti₂₁Zr₂₁Fe₄₁Ni₁₇ Medium Entropy Alloy, ACS Applied Energy Materials 8 (4) (2025) 2033– 2042, publisher: American Chemical Society. doi:10.1021/ acsaem.4c02468.
 - URL https://doi.org/10.1021/acsaem.4c02468
- Y. Osumi, H. Suzuki, A. Kato, K. Oguro, T. Sugioka, T. Fujita, Hydrogen storage properties of Ti_{1+x}Cr_{2-y}Mn_y alloys, Journal of the Less Common Metals 89 (1) (1983) 257-262. doi:10.1016/0022-5088(83)90277-1.
 URL https://linkinghub.elsevier.com/retrieve/pii/
 - URL https://linkinghub.elsevier.com/retrieve/pii/
 0022508883902771

- [10] K. Manickam, D. M. Grant, G. S. Walker, Optimization of AB₂ type alloy composition with superior hydrogen storage properties for stationary applications, International Journal of Hydrogen Energy 40 (46) (2015) 16288-16296. doi:10.1016/j.ijhydene.2015.09.157.
 - URL https://linkinghub.elsevier.com/retrieve/pii/ S0360319915024878
- [11] B. Villeroy, F. Cuevas, J. Bettembourg, P. Olier, M. Latroche, Influence of the Ti/Zr ratio and the synthesis route on hydrogen absorbing properties of $(Ti_{1-x}Zr_x)Mn_{1.5}V_{0.5}$ alloys, Journal of Physics and Chemistry of Solids 67 (5-6) (2006) 1281–1285. doi:10.1016/j.jpcs.2006.01.058. https://linkinghub.elsevier.com/retrieve/pii/ S0022369706000862
- [12] J. R. Johnson, J. J. Reilly, Reaction of hydrogen with the low-temperature form (C15) of titanium-chromium (TiCr₂), Inorganic Chemistry 17 (11) (1978) 3103-3108. doi:10.1021/ ic50189a027.
 - URL https://pubs.acs.org/doi/abs/10.1021/ic50189a027
- [13] J. R. Johnson, Reaction of hydrogen with the high temperature (C14) form of TiCr₂, Journal of the Less Common Metals 73 (2) $(1980)\ 345-354.\ {\tt doi:10.1016/0022-5088(80)90328-8}.$ URL https://www.sciencedirect.com/science/article/pii/ 0022508880903288
- [14] A. J. McGrath, M. D. Wadge, M. Adams, K. Manickam, S. Ling, G. S. Walker, D. M. Grant, Stoichiometry and annealing condition on hydrogen capacity of ${\rm TiCr_{2-x}}$ ${\rm AB_2}$ alloys, International Journal of Hydrogen Energy 53 (2024) 582–591. doi:10.1016/j.ijhydene.2023.12.062. URL https://www.sciencedirect.com/science/article/pii/ S0360319923063620
- [15] F. Agresti, S. Lo Russo, A. Maddalena, G. Principi, G. Mazzolai, B. Coluzzi, A. Biscarini, F. Mazzolai, A. Tuissi, Reaction of hydrogen with the Laves phase (C14) $TiCr_{1.78-x}Mn_x$ compounds, Materials Science and Engineering: A 521-522 (2009) 143-146. doi:10.1016/j.msea.2008.09.154. https://linkinghub.elsevier.com/retrieve/pii/ S0921509309002652
- [16] W. Jiang, C. He, X. Yang, X. Xiao, L. Ouyang, M. Zhu, Influence of element substitution on structural stability and hydrogen storage performance: A theoretical and experimental study on TiCr_{2-x}Mn_x alloy, Renewable Energy 197 (2022) 564-573. doi:10.1016/j.renene.2022.07.113. URL https://www.sciencedirect.com/science/article/pii/ S0960148122011156
- [17] R. C. Bowman, B. D. Craft, A. Attalla, J. R. Johnson, Diffusion behavior in titanium-chromium hydrides, International Journal of Hydrogen Energy 8 (10) (1983) 801-808. doi: 10.1016/0360-3199(83)90211-2. URL https://www.sciencedirect.com/science/article/pii/ 0360319983902112
- [18] S. I. Campbell, M. Kemali, D. K. Ross, D. J. Bull, J. F. Fernandez, M. R. Johnson, Quasi-elastic neutron scattering study of the hydrogen diffusion in the C15 Laves structure, TiCr_{1.85}, Journal of Alloys and Compounds 293-295 (1999) 351-355. doi:10.1016/S0925-8388(99)00400-4.
 - URL https://www.sciencedirect.com/science/article/pii/ S0925838899004004
- [19] G. Mazzolai, B. Coluzzi, A. Biscarini, F. M. Mazzolai, A. Tuissi, F. Agresti, G. Principi, S. Lo Russo, Hydrogen diffusion in the Laves-phase compound TiCr_{1.78}, Materials Science and Engineering: A 521-522 (2009) 139-142. doi:10.1016/j.msea.2008. 09.108.
 - URL https://www.sciencedirect.com/science/article/pii/ S0921509309002640
- [20] K. Hiebl, Proton and deuteron nuclear magnetic resonance studies of TiCr_{1.85}H_x(D_x), Materials Research Bulletin 17 (6) $(1982)\ 757-761.\ {\tt doi:10.1016/0025-5408(82)90026-5}.$ URL https://www.sciencedirect.com/science/article/pii/ 0025540882900265
- [21] F. Li, J. Zhao, D. Tian, H. Zhang, X. Ke, B. Johansson, Hy-

- drogen storage behavior in C15 Laves phase compound TiCr₂ by first principles, Journal of Applied Physics 105 (4) (2009) 043707. doi:10.1063/1.3081636.URL https://doi.org/10.1063/1.3081636
- [22] K. Miwa, R. Asahi, Path integral study on C15-type Laves TiCr₂ hydride, International Journal of Hydrogen Energy 44 (42) (2019) 23708-23715. doi:10.1016/j.ijhydene.2019. 07.086.
 - URL https://www.sciencedirect.com/science/article/pii/ S0360319919326618
- [23] S. M. Loh, D. M. Grant, G. S. Walker, S. Ling, Substitutional effect of Ti-based AB₂ hydrogen storage alloys: A density functional theory study, International Journal of Hydrogen Energy 48 (35) (2023) 13227-13235. doi:10.1016/j.ijhydene.2022. URL https://www.sciencedirect.com/science/article/pii/
- [24] N. Wang, S. Huang, Molecular dynamics study on magnesium hydride nanoclusters with machine-learning interatomic potential, Physical Review B 102 (9) (2020) 094111. doi:10.1103/PhysRevB.102.094111. https://link.aps.org/doi/10.1103/PhysRevB.102. URL 094111

S0360319922057998

- [25] H. Kwon, M. Shiga, H. Kimizuka, T. Oda, Accurate description of hydrogen diffusivity in bcc metals using machine-learning moment tensor potentials and path-integral methods, Acta Materialia 247 (2023) 118739. doi:10.1016/j.actamat.2023.118739. URL https://www.sciencedirect.com/science/article/pii/ S135964542300071X
- [26] J. Qi, T. W. Ko, B. C. Wood, T. A. Pham, S. P. Ong, Robust training of machine learning interatomic potentials with dimensionality reduction and stratified sampling, npj Computational Materials 10 (1) (2024) 1-11, publisher: Nature Publishing Group. doi:10.1038/s41524-024-01227-4.
- URL https://www.nature.com/articles/s41524-024-01227-4 [27] F. Yu, X. Xiang, X. Zu, S. Hu, Hydrogen diffusion in zirconium hydrides from on-the-fly machine learning molecular dynamics, International Journal of Hydrogen Energy 56 (2024) 1057–1066. doi:10.1016/j.ijhydene.2023.12.241. URL https://www.sciencedirect.com/science/article/pii/ S0360319923065424
- [28] A. Angeletti, L. Leoni, D. Massa, L. Pasquini, S. Papanikolaou, C. Franchini, Hydrogen diffusion in magnesium using machine learning potentials: a comparative study, npj Computational Materials 11 (1) (2025) 85. doi:10.1038/s41524-025-01555-z. URL https://www.nature.com/articles/s41524-025-01555-z
- [29] O. Morrison, E. Uteva, G. S. Walker, D. M. Grant, S. Ling, Long Time Scale Molecular Dynamics Simulation of Magnesium Hydride Dehydrogenation Enabled by Machine Learning Interatomic Potentials, ACS Applied Energy Materials 8 (1) (2025) 492-502. doi:10.1021/acsaem.4c02627.
 - URL https://pubs.acs.org/doi/10.1021/acsaem.4c02627
- Y. Ou, Y. Ikeda, L. Scholz, S. Divinski, F. Fritzen, B. Grabowski, Atomistic modeling of bulk and grain boundary diffusion in solid electrolyte Li₆PS₅Cl using machine-learning interatomic potentials, Physical Review Materials 8 (11) (2024) 115407, publisher: American Physical Society. doi:10.1103/ PhysRevMaterials.8.115407.
 - $\label{eq:url_link} URL~ \texttt{https://link.aps.org/doi/10.1103/PhysRevMaterials.}$ 8.115407
- [31] Y. Ou, L. Scholz, S. Keshav, Y. Ikeda, M. Kraft, S. Divinski, R. Gómez-Bombarelli, W. G. Zeier, F. Fritzen, B. Grabowski, Non-Arrhenius Li-ion transport and grain-size effects in argyrodite solid electrolytes, version Number: 1 (2025). doi: 10.48550/ARXIV.2510.18630. URL https://arxiv.org/abs/2510.18630
- [32] P. Kumar, F. Körmann, B. Grabowski, Y. Ikeda, Machine learning potentials for hydrogen absorption in TiCr₂ Laves phases, Acta Materialia 297 (2025) 121319. doi:https://doi.org/10. 1016/j.actamat.2025.121319.
 - URL https://www.sciencedirect.com/science/article/pii/

S1359645425006056

- [33] D. P. Shoemaker, C. B. Shoemaker, Concerning atomic sites and capacities for hydrogen absorption in the AB₂ Friauf-Laves phases, Journal of the Less Common Metals 68 (1) (1979) 43– 58. doi:10.1016/0022-5088(79)90271-6. URL https://www.sciencedirect.com/science/article/pii/ 0022508879902716
- [34] D. Thoma, J. Perepezko, A geometric analysis of solubility ranges in Laves phases, Journal of Alloys and Compounds 224 (2) (1995) 330-341. doi:10.1016/0925-8388(95)01557-4. URL https://linkinghub.elsevier.com/retrieve/pii/0925838895015574
- [35] K. C. Chen, S. M. Allen, J. D. Livingston, Stoichiometry and Alloying Effects on the Phase Stability and Mechanical Properties of TiCr₂-Base Laves Phase Alloys, MRS Online Proceedings Library 364 (1) (1994) 1401–1406. doi:10.1557/PROC-364-1401. URL https://doi.org/10.1557/PROC-364-1401
- [36] J. L. Murray, The Cr-Ti (chromium-titanium) system, Bulletin of Alloy Phase Diagrams 2 (2) (1981) 174-181. doi:10.1007/ BF02881474. URL https://doi.org/10.1007/BF02881474
- [37] M. Sluiter, P. E. A. Turchi, Phase stability in Ti-V and Ti-Cr alloys: A theoretical investigation, Physical Review B 43 (15) (1991) 12251-12266. doi:10.1103/PhysRevB.43.12251. URL https://link.aps.org/doi/10.1103/PhysRevB.43.12251
- [38] A. M. Mebed, T. Miyazaki, Computer simulation and experimental investigation of the spinodal decomposition in the β Ti-Cr binary alloy system, Metallurgical and Materials Transactions A 29 (3) (1998) 739–749. doi:10.1007/s11661-998-0264-1. URL https://doi.org/10.1007/s11661-998-0264-1
- [39] J. Furthmüller, J. Hafner, G. Kresse, Dimer reconstruction and electronic surface states on clean and hydrogenated diamond (100) surfaces, Physical Review B 53 (11) (1996) 7334–7351, publisher: American Physical Society. doi:10.1103/PhysRevB. 53.7334.
- URL https://link.aps.org/doi/10.1103/PhysRevB.53.7334
 [40] G. Kresse, J. Furthmüller, Efficiency of ab-initio total energy calculations for metals and semiconductors using a plane-wave basis set, Computational Materials Science 6 (1) (1996) 15-50. doi:10.1016/0927-0256(96)00008-0.

 URL https://www.sciencedirect.com/science/article/pii/0927025696000080
- [41] G. Kresse, D. Joubert, From ultrasoft pseudopotentials to the projector augmented-wave method, Physical Review B 59 (3) (1999) 1758–1775, publisher: American Physical Society. doi: 10.1103/PhysRevB.59.1758.
- URL https://link.aps.org/doi/10.1103/PhysRevB.59.1758
 [42] P. E. Blöchl, Projector augmented-wave method, Physical Review B 50 (24) (1994) 17953–17979, publisher: American Physical Society. doi:10.1103/PhysRevB.50.17953.
- URL https://link.aps.org/doi/10.1103/PhysRevB.50.17953
 [43] J. P. Perdew, K. Burke, M. Ernzerhof, Generalized Gradient Approximation Made Simple, Physical Review Letters 77 (18) (1996) 3865-3868, publisher: American Physical Society. doi:10.1103/PhysRevLett.77.3865.
 URL https://link.aps.org/doi/10.1103/PhysRevLett.77.
- [44] M. Methfessel, A. T. Paxton, High-precision sampling for Brillouin-zone integration in metals, Physical Review B 40 (6) (1989) 3616-3621, publisher: American Physical Society. doi: 10.1103/PhysRevB.40.3616. URL https://link.aps.org/doi/10.1103/PhysRevB.40.3616
- [45] D. Sheppard, P. Xiao, W. Chemelewski, D. D. Johnson, G. Henkelman, A generalized solid-state nudged elastic band method, The Journal of Chemical Physics 136 (7) (2012) 074103. doi:10.1063/1.3684549. URL https://pubs.aip.org/jcp/article/136/7/074103/ 190791/A-generalized-solid-state-nudged-elastic-band
- [46] G. Henkelman, B. P. Uberuaga, H. Jónsson, A climbing image nudged elastic band method for finding saddle points and min-

- imum energy paths, The Journal of Chemical Physics 113 (22) (2000) 9901–9904. doi:10.1063/1.1329672. URL https://doi.org/10.1063/1.1329672
- [47] G. Henkelman, H. Jónsson, Improved tangent estimate in the nudged elastic band method for finding minimum energy paths and saddle points, The Journal of Chemical Physics 113 (22) (2000) 9978–9985. doi:10.1063/1.1323224. URL https://doi.org/10.1063/1.1323224
- [48] D. Sheppard, R. Terrell, G. Henkelman, Optimization methods for finding minimum energy paths, The Journal of Chemical Physics 128 (13) (2008) 134106. doi:10.1063/1.2841941. URL https://pubs.aip.org/jcp/article/128/13/134106/ 977389/Optimization-methods-for-finding-minimum-energy
- [49] A. V. Shapeev, Moment Tensor Potentials: A Class of Systematically Improvable Interatomic Potentials, Multiscale Modeling & Simulation 14 (3) (2016) 1153-1173, publisher: Society for Industrial and Applied Mathematics. doi:10.1137/15M1054183. URL https://epubs.siam.org/doi/10.1137/15M1054183
- [50] E. V. Podryabinkin, A. V. Shapeev, Active learning of linearly parametrized interatomic potentials, Computational Materials Science 140 (2017) 171-180. doi:10.1016/j.commatsci.2017. 08.031.
 - URL https://www.sciencedirect.com/science/article/pii/ S0927025617304536
- [51] K. Gubaev, E. V. Podryabinkin, G. L. W. Hart, A. V. Shapeev, Accelerating high-throughput searches for new alloys with active learning of interatomic potentials, Computational Materials Science 156 (2019) 148-156. doi:10.1016/j.commatsci.2018. 09.031. URL https://www.sciencedirect.com/science/article/pii/
- [52] E. Podryabinkin, K. Garifullin, A. Shapeev, I. Novikov, MLIP-3: Active learning on atomic environments with moment tensor potentials, The Journal of Chemical Physics 159 (8) (2023) 084112. doi:10.1063/5.0155887.
 URL https://doi.org/10.1063/5.0155887

S0927025618306372

- [53] A. Einstein, Über die von der molekularkinetischen Theorie der Wärme geforderte Bewegung von in ruhenden Flüssigkeiten suspendierten Teilchen, Annalen der Physik 322 (8) (1905) 549– 560. doi:10.1002/andp.19053220806. URL https://onlinelibrary.wiley.com/doi/10.1002/andp. 19053220806
- [54] A. P. Thompson, H. M. Aktulga, R. Berger, D. S. Bolintineanu, W. M. Brown, P. S. Crozier, P. J. In 'T Veld, A. Kohlmeyer, S. G. Moore, T. D. Nguyen, R. Shan, M. J. Stevens, J. Tranchida, C. Trott, S. J. Plimpton, LAMMPS a flexible simulation tool for particle-based materials modeling at the atomic, meso, and continuum scales, Computer Physics Communications 271 (2022) 108171. doi:10.1016/j.cpc.2021.108171. URL https://linkinghub.elsevier.com/retrieve/pii/S0010465521002836
- [55] I. S. Novikov, K. Gubaev, E. V. Podryabinkin, A. V. Shapeev, The MLIP package: moment tensor potentials with MPI and active learning, Machine Learning: Science and Technology 2 (2) (2020) 025002, publisher: IOP Publishing. doi:10.1088/ 2632-2153/abc9fe. URL https://dx.doi.org/10.1088/2632-2153/abc9fe
- [56] Z. Meng, K. Zongo, E. Torres, C. Maxwell, R. E. Grant, L. K. Béland, A Kokkos-Accelerated Moment Tensor Potential Implementation for LAMMPS, version Number: 1 (2025). doi:10.48550/ARXIV.2510.00193. URL https://arxiv.org/abs/2510.00193
- [57] L. J. Lauhon, W. Ho, Direct Observation of the Quantum Tunneling of Single Hydrogen Atoms with a Scanning Tunneling Microscope, Physical Review Letters 85 (21) (2000) 4566-4569. doi:10.1103/PhysRevLett.85.4566.
 URL https://link.aps.org/doi/10.1103/PhysRevLett.85.4566
- [58] C. Z. Zheng, C. K. Yeung, M. M. T. Loy, X. Xiao, Quantum Diffusion of H on Pt(111): Step Effects, Physical Review Letters

- 97 (16) (2006) 166101. doi:10.1103/PhysRevLett.97.166101. URL https://link.aps.org/doi/10.1103/PhysRevLett.97.166101
- [59] H. Kimizuka, H. Mori, S. Ogata, Effect of temperature on fast hydrogen diffusion in iron: A path-integral quantum dynamics approach, Physical Review B 83 (9) (2011) 094110. doi:10.1103/PhysRevB.83.094110.
 - URL https://link.aps.org/doi/10.1103/PhysRevB.83.
 094110
- [60] D. Di Stefano, M. Mrovec, C. Elsässer, First-principles investigation of quantum mechanical effects on the diffusion of hydrogen in iron and nickel, Physical Review B 92 (22) (2015) 224301. doi:10.1103/PhysRevB.92.224301. URL https://link.aps.org/doi/10.1103/PhysRevB.92.
- [61] S. Duane, A. Kennedy, B. J. Pendleton, D. Roweth, Hybrid Monte Carlo, Physics Letters B 195 (2) (1987) 216-222. doi:10.1016/0370-2693(87)91197-X. URL https://linkinghub.elsevier.com/retrieve/pii/ 037026938791197X

224301

- [62] M. E. Tuckerman, B. J. Berne, G. J. Martyna, M. L. Klein, Efficient molecular dynamics and hybrid Monte Carlo algorithms for path integrals, The Journal of Chemical Physics 99 (4) (1993) 2796-2808. doi:10.1063/1.465188. URL https://pubs.aip.org/jcp/article/99/4/2796/859202/Efficient-molecular-dynamics-and-hybrid-Monte
- [63] B. Mehlig, D. W. Heermann, B. M. Forrest, Hybrid Monte Carlo method for condensed-matter systems, Physical Review B 45 (2) (1992) 679-685. doi:10.1103/PhysRevB.45.679. URL https://link.aps.org/doi/10.1103/PhysRevB.45.679
- [64] Z. Li, H. Wang, L. Ouyang, J. Liu, M. Zhu, Achieving superior de-/hydrogenation properties of C15 Laves phase Y-Fe-Al alloys by A-side substitution, Journal of Alloys and Compounds 787 (2019) 158-164. doi:10.1016/j.jallcom.2019.02.074. URL https://www.sciencedirect.com/science/article/pii/ S0925838819305146
- [65] S. B. Gesari, M. E. Pronsato, A. Visintin, A. Juan, Hydrogen Storage in AB₂ Laves Phase (A = Zr, Ti; B = Ni, Mn, Cr, V): Binding Energy and Electronic Structure, The Journal of Physical Chemistry C 114 (39) (2010) 16832–16836, publisher: American Chemical Society. doi:10.1021/jp106036v. URL https://doi.org/10.1021/jp106036v
- [66] A. R. Merlino, C. R. Luna, A. Juan, M. E. Pronsato, A DFT study of hydrogen storage in Zr(Cr_{0.5}Ni_{0.5})₂ Laves phase, International Journal of Hydrogen Energy 41 (4) (2016) 2700-2710. doi:10.1016/j.ijhydene.2015.10.077. URL https://www.sciencedirect.com/science/article/pii/S036031991530968X
- [67] H. W. Kroto, The stability of the fullerenes C_n , with n=24, 28, 32, 36, 50, 60 and 70, Nature 329 (6139) (1987) 529–531. doi:10.1038/329529a0.
- URL https://www.nature.com/articles/329529a0
 [68] E. C. J. Gießelmann, R. Pöttgen, O. Janka, Laves phases: superstructures induced by coloring and distortions, Zeitschrift für anorganische und allgemeine Chemie 649 (16) (2023) e202300109. doi:10.1002/zaac.202300109. URL https://onlinelibrary.wiley.com/doi/10.1002/zaac.202300109
- [69] A. V. Skripov, Hydrogen diffusion in Laves-phase compounds, in: Defect and Diffusion Forum, Vol. 224, Trans Tech Publ, 2003, pp. 75–92.
- [70] X. Zhong, F. Höfling, T. John, Hydrogen Diffusion in Garnet: Insights From Atomistic Simulations, Geochemistry, Geophysics, Geosystems 26 (2) (2025) e2024GC011951.
 doi:10.1029/2024GC011951.
 URL https://agupubs.onlinelibrary.wiley.com/doi/10.1029/2024GC011951
- [71] H. Kimizuka, S. Ogata, M. Shiga, Mechanism of fast lattice diffusion of hydrogen in palladium: Interplay of quantum fluctuations and lattice strain, Physical Review B 97 (1) (2018) 014102. doi:10.1103/PhysRevB.97.014102.

- URL https://link.aps.org/doi/10.1103/PhysRevB.97.
 014102
- [72] B. Grabowski, T. Hickel, J. Neugebauer, Ab initio study of the thermodynamic properties of nonmagnetic elementary fcc metals: Exchange-correlation-related error bars and chemical trends, Physical Review B 76 (2) (2007) 024309. doi:10.1103/PhysRevB.76.024309. URL https://link.aps.org/doi/10.1103/PhysRevB.76. 024309

Hydrogen diffusion in $TiCr_2H_x$ Laves phases: A combined *ab initio* and machine-learning-potential study

Supplementary Materials

S1. Minimum-Energy Paths

Figure S1 presents the minimum-energy paths for all symmetrically inequivalent paths of $TiCr_2$ in the C15 cubic and the C14 hexagonal Laves phases obtained with DFT in conjunction with the G-SSNEB method.

S2. Comparison of G-SSNEB Migration Barriers from DFT and MTP

Table S1 presents a comparison of the G-SSNEB migration barriers obtained from the trained MTPs alongside the corresponding DFT values (Table 3 in the main text). The G-SSNEB calculations were performed within ASE [S1] using the TSASE library (https://theory.cm.utexas.edu/tsase/), employing the same G-SSNEB settings as DFT described in Sec. 3.2 in the main text.

The MTPs well reproduce the trend obtained from DFT. Particularly, a Ti–H bond requires a higher energy to break than a Cr–H bond. Specifically, the migration energies involving the breaking of a Ti–H bond span 282–739 meV and 233–723 meV for the C15 and the C14 phases, respectively. In contrast, the migration energies involving the breaking of a Cr–H bond span 119–196 meV and 80–138 meV for the C15 and the C14 phases, respectively. The RMSEs of the MTP prediction are 27 meV for both the C15 and the C14 phases.

Table S1: Hydrogen migration energies for all symmetry-distinct diffusion paths in the TiCr₂ Laves phases obtained with the MTPs. The DFT values are also shown in parentheses for comparison. The "Face" column indicates the common face between two interstitial sites through which hydrogen migrates. The "Bond breaking" columns specify the types of metal–hydrogen bond broken during migration.

	S_1	S_2		Bond breaking		$E_{\rm mig}~({\rm meV})$	
	~ I	<i>2</i>	Face	$S_1 \to S_2$	$S_2 \to S_1$	$S_1 \to S_2$	$S_2 \to S_1$
C15	8b (B ₄)	$32e \text{ (AB}_3)$	B_3	В–Н	A-H	190	805
	32e (AB ₃)	$96g (A_2B_2)$	AB_2	В–Н	A-H	90	291
	$96g (A_2B_2)$	$96g (A_2B_2)$	AB_2	A-H	A-H	286	286
	$96g (A_2B_2)$	$96g (A_2B_2)$	A_2B	В–Н	В–Н	119	119
C14	4e (B ₄)	4e (B ₄)	B_3	В–Н	В–Н	154	154
	4e (B ₄)	$12k_1 \text{ (AB}_3)$	B_3	В–Н	A-H	154	739
	4f (AB ₃)	4f (AB ₃)	B_3	A-H	A-H	635	635
	4f (AB ₃)	$12k_2 \left(\mathbf{A_2} \mathbf{B_2} \right)$	AB_2	В–Н	A-H	111	362
	$12k_1 \text{ (AB}_3)$	$6h_1 (A_2B_2)$	AB_2	В–Н	A-H	98	249
	$12k_1 \text{ (AB}_3)$	$24l (A_2B_2)$	AB_2	В–Н	A-H	97	264
	$6h_1 (A_2B_2)$	$6h_2 (A_2B_2)$	A_2B	В–Н	В–Н	86	165
	$6h_2 \ (A_2B_2)$	$12k_2 \ (A_2B_2)$	AB_2	A-H	A-H	280	203
	$12k_2 (A_2B_2)$	$24l (A_2B_2)$	A_2B	В–Н	В–Н	111	123
	$24l (A_2B_2)$	$24l (A_2B_2)$	AB_2	A-H	A-H	314	314
	$24l (A_2B_2)$	$24l (A_2B_2)$	A_2B	В–Н	В–Н	99	99

S3. Evolution of mean squared displacements

Figure S2 illustrates the evolution of the MSD of hydrogen in $TiCr_2H_x$ over MD time at five different temperatures: $250 \, \text{K}$, $400 \, \text{K}$, $500 \, \text{K}$, $750 \, \text{K}$, and $1000 \, \text{K}$.

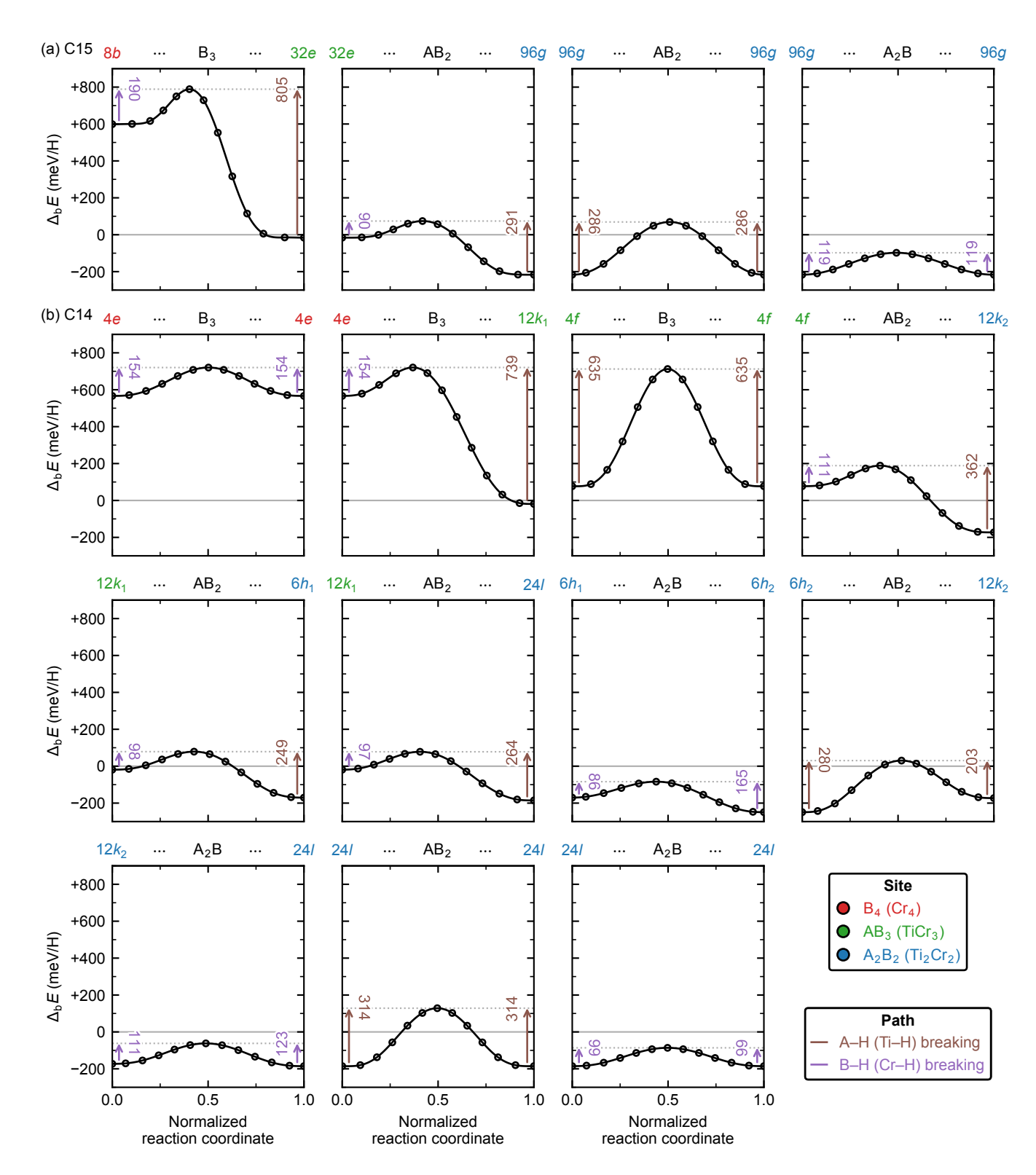


Figure S1: Minimum-energy paths for all symmetrically inequivalent paths of $TiCr_2$ in the (a) C15 cubic and the (b) C14 hexagonal Laves phases obtained with DFT in conjunction with the G-SSNEB method.

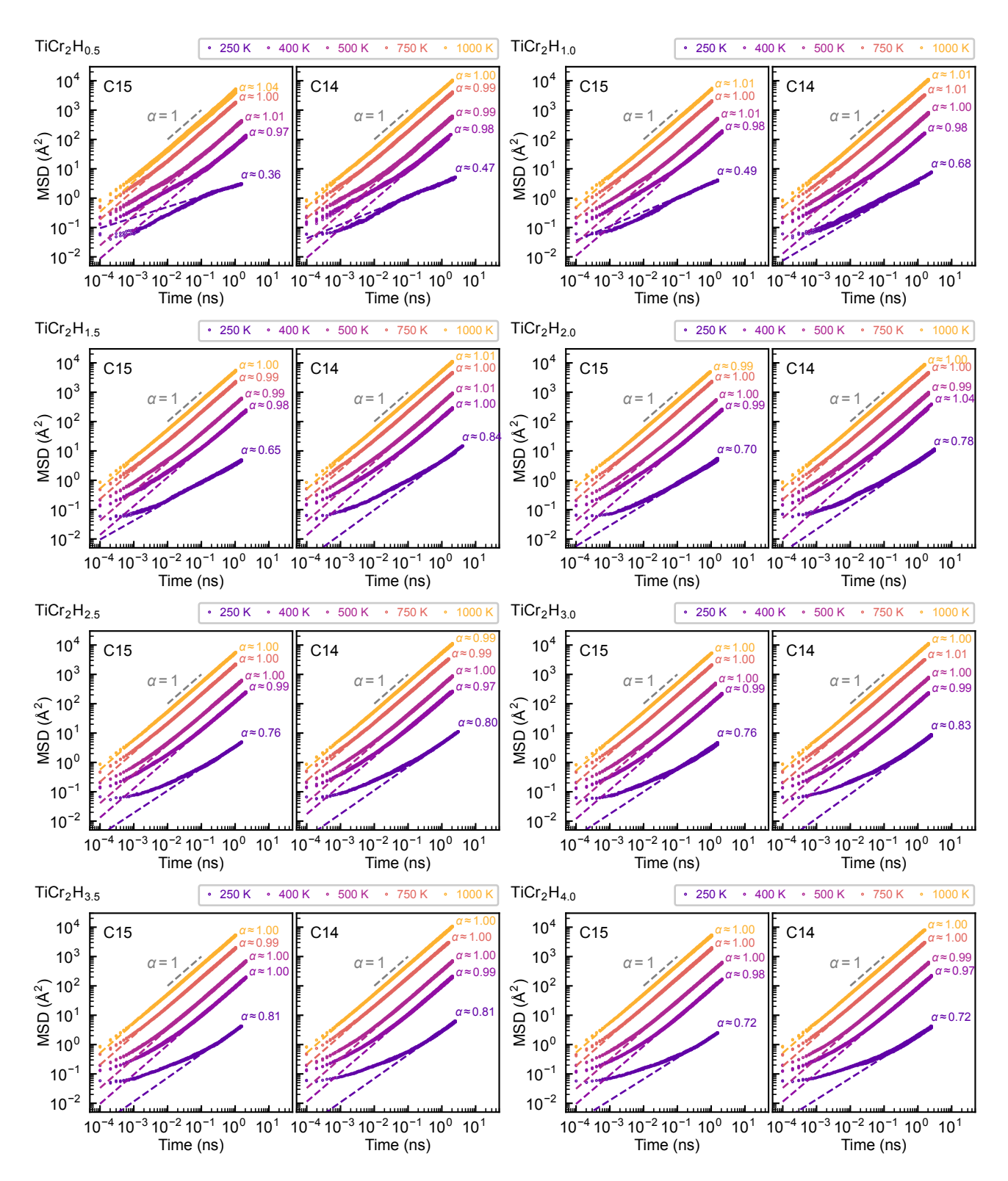


Figure S2: MSDs of hydrogen atoms in $TiCr_2H_x$ as a function of MD simulation time.

S4. Diffusion coefficients

Tables S2 and S3 present the diffusion coefficients of ${\rm TiCr_2H_x}$ obtained with the MD simulations.

Table S2: Diffusion coefficients ($10^{-7}\,\mathrm{cm^2/s}$) of C15 $\mathrm{TiCr_2H_x}$ obtained with the MD simulations.

	T (K)	x	MD1	MD2	MD3	MD4	MD5	Mean	SD
C15	400	0.5	10.133	11.256	10.828	10.612	10.818	10.729	0.364
		1.0	15.779	15.118	14.691	15.142	14.508	15.047	0.440
		1.5	19.651	18.644	19.541	18.708	18.333	18.975	0.523
		2.0	19.931	20.669	21.436	20.972	21.208	20.843	0.522
		2.5	20.335	19.910	20.154	19.876	20.920	20.239	0.380
		3.0	17.759	17.562	18.469	17.588	18.425	17.961	0.403
		3.5	16.132	16.327	15.682	15.371	15.470	15.797	0.373
		4.0	13.514	14.194	13.462	13.482	13.404	13.611	0.293
	500	0.5	43.836	47.473	45.115	46.148	46.425	45.799	1.236
		1.0	54.713	54.713	56.394	57.251	53.628	55.340	1.302
		1.5	65.037	64.159	63.873	65.474	66.249	64.958	0.867
		2.0	67.204	67.216	68.401	67.204	67.216	67.448	0.476
		2.5	66.011	67.061	64.694	68.573	65.918	66.451	1.299
		3.0	60.746	61.002	60.497	57.662	60.344	60.050	1.215
		3.5	54.468	56.515	57.206	54.342	56.848	55.876	1.221
		4.0	51.039	52.630	53.022	51.430	51.375	51.899	0.779
	750	0.5	294.454	300.831	305.091	299.971	288.792	297.828	5.646
		1.0	330.314	338.418	332.833	338.007	320.336	331.982	6.585
		1.5	350.125	367.585	363.297	348.385	352.306	356.340	7.655
		2.0	371.810	368.607	377.147	367.596	363.333	369.699	4.606
		2.5	367.617	354.307	363.309	356.141	360.240	360.323	4.813
		3.0	345.693	351.547	346.552	347.483	338.582	345.972	4.204
		3.5	322.819	331.094	319.180	318.423	337.587	325.821	7.404
		4.0	315.755	299.955	308.442	317.930	320.202	312.457	7.392
	1000	0.5	801.825	829.650	832.483	802.807	871.537	827.660	25.446
		1.0	863.952	856.831	856.839	848.338	886.754	862.543	13.077
		1.5	898.824	904.457	891.629	877.511	903.267	895.138	9.895
		2.0	926.771	900.716	897.442	902.577	909.486	907.398	10.456
		2.5	922.420	900.865	893.941	911.371	904.076	906.535	9.721
		3.0	894.984	880.986	900.187	883.554	898.665	891.675	7.905
		3.5	867.791	887.523	898.665	870.310	896.538	884.165	12.920
		4.0	888.874	875.564	894.710	845.373	891.865	879.277	18.177

Table S3: Diffusion coefficients $(10^{-7} \, \mathrm{cm^2/s})$ of C14 $\mathrm{TiCr_2H_x}$ obtained with the MD simulations.

	T (K)	x	MD1	MD2	MD3	MD4	MD5	Mean	SD
C14	400	0.5	14.344	13.564	13.411	13.154	12.154	13.326	0.708
		1.0	18.460	17.615	17.913	17.917	17.592	17.899	0.313
		1.5	22.131	22.610	23.087	23.812	22.236	22.775	0.617
		2.0	23.910	23.389	25.452	24.302	22.825	23.976	0.890
		2.5	22.056	24.177	21.610	22.654	22.233	22.546	0.882
		3.0	19.256	19.484	20.187	19.501	18.795	19.445	0.450
		3.5	15.925	16.742	16.766	17.140	17.523	16.819	0.530
		4.0	15.068	14.066	14.423	14.875	14.847	14.656	0.362
	500	0.5	46.090	51.443	47.042	45.522	46.270	47.273	2.141
		1.0	67.638	62.584	64.206	61.558	62.591	63.715	2.137
		1.5	72.044	74.203	72.824	71.802	70.507	72.276	1.218
		2.0	80.570	79.830	77.043	75.387	71.707	76.908	3.204
		2.5	72.236	68.354	70.882	72.121	71.528	71.024	1.419
		3.0	61.677	64.010	63.500	62.451	61.301	62.588	1.035
		3.5	57.026	57.653	56.352	55.087	55.507	56.325	0.944
		4.0	50.857	52.983	53.515	50.094	50.435	51.577	1.396
	750	0.5	315.832	326.092	329.621	338.672	319.363	325.916	8.014
		1.0	366.231	349.263	364.663	352.065	353.294	357.103	6.955
		1.5	376.589	377.106	375.775	380.565	381.136	378.234	2.185
		2.0	381.543	371.881	372.906	382.447	369.274	375.610	5.354
		2.5	379.671	364.795	366.926	380.577	373.034	373.001	6.421
		3.0	351.194	351.553	353.284	353.786	344.733	350.910	3.242
		3.5	326.387	328.774	342.707	335.671	336.342	333.976	5.820
		4.0	309.857	320.603	315.014	323.485	325.319	318.856	5.692
	1000	0.5	833.150	827.726	834.807	830.568	829.881	831.226	2.491
		1.0	887.020	896.067	900.972	884.110	855.862	884.806	15.692
		1.5	912.921	921.323	894.645	888.604	896.125	902.724	12.313
		2.0	935.324	937.033	915.019	937.695	908.690	926.752	12.352
		2.5	918.788	894.380	895.554	931.341	916.876	911.388	14.304
		3.0	887.772	914.446	906.416	920.082	900.757	905.895	11.221
		3.5	865.096	895.785	900.924	885.466	895.355	888.525	12.739
		4.0	898.837	868.894	885.213	885.991	894.711	886.729	10.308

References

[S1] A. H. Larsen, J. J. Mortensen, J. Blomqvist, I. E. Castelli, R. Christensen, M. Dułak, J. Friis, M. N. Groves, B. Hammer, C. Hargus, E. D. Hermes, P. C. Jennings, P. B. Jensen, J. Kermode, J. R. Kitchin, E. L. Kolsbjerg, J. Kubal, K. Kaasbjerg, S. Lysgaard, J. B. Maronsson, T. Maxson, T. Olsen, L. Pastewka, A. Peterson, C. Rostgaard, J. Schiøtz, O. Schütt, M. Strange, K. S. Thygesen, T. Vegge, L. Vilhelmsen, M. Walter, Z. Zeng, K. W. Jacobsen, The atomic simulation environment—a Python library for working with atoms, Journal of Physics: Condensed Matter 29 (2017) 273002. doi:10.1088/1361-648X/aa680e.